NIST Advanced Manufacturing Series 100-6

Effects of powder recycling on stainless steel powder and built material properties in metal powder bed fusion processes

Gregor Jacob
Christopher Brown
Alkan Donmez
Stephanie Watson
John Slotwinski

NIST

National Institute of
Standards and Technology
U.S. Department of Commerce

NIST Advanced Manufacturing Series 100-6

Effects of powder recycling on stainless steel powder and built material properties in metal powder bed fusion processes

Gregor Jacob
Christopher Brown
Alkan Donmez
Stephanie Watson
Engineering Laboratory

John Slotwinski
Applied Physics Laboratory
The Johns Hopkins University

February 2017

Abstract

A series of 11 identical laser-based powder bed fusion (PBF) builds were completed with varying amounts of virgin and recycled nitrogen gas atomized S17-4 PH stainless steel powder following a specific powder recycling strategy that simulates industrial practice. Mechanical properties of parts were evaluated using tensile and hardness tests. Recycled powder properties, such as particle size distribution, flowability, chemical composition, and microstructure were evaluated. The recycled powder showed no significant changes in its particle size (PS), particle size distribution (PSD), and particle shape but apparent density and powder bed density increased while flow time improved. Recycling the powder in a nitrogen atmosphere caused a slight increase of the martensitic-ferritic phase in the predominately austenitic S17-4 PH powder. Laser-based PBF fabricated austenitic-martensitic-ferritic S17-4 PH showed a ratio of approximately 1:1 between austenitic and martensitic-ferritic phases. The specimens were heat treated for stress relief. Tensile tests on the specimens did not show dramatic change in the tensile properties with recycling up to 11 times. The fine dendritic austenitic-martensitic-ferritic microstructure of the heat-treated S17-4-PH reached a 0.2 % offset yield strength ($YS_{0.2}$) above 520 MPa, and an elongation after fracture (A) of 28 %. Mechanical and material properties from specimens fabricated from powder recycled up to 11 times were similar to specimens fabricated from virgin powder.

Disclaimer

Table of Contents

List of Figures

List of Tables

1. Introduction

The influence of the characteristics of metal powder used for powder bed fusion (PBF) [*ASTM F2792, 2012*] processes on the final mechanical or material properties is not well understood. It is reported in literature that powder characteristics affect the governing thermal properties during the PBF process resulting in varying material properties of the final product, but such relationships are not well established [*Karapatis et al, 1999, Dingal et al, 2008, Spierings and Levy, 2009, Liu et al, 2011, Spierings et al, 2011, Averyanova et al, 2012, Olakanmi 2013, Gu et al, 2015, and Engeli et al, 2016*]. Another unknown in the relationship between powder characteristics and the final material properties is the effect of the condition of the powder after several reuses or recycles. It is a common practice to use un-melted metal powder from prior builds or to mix such powder with virgin powder in additive manufacturing (AM) processes to reduce the cost of AM parts. Understanding the condition of the metal powder before a build, and its impact on the final part properties, are important to advance our understanding of the PBF systems.

In most PBF machines powder is supplied from a dispenser bin to the build platform. The required thickness of powder layer is spread using a recoating mechanism by adjusting the height of the build platform with respect to the recoating mechanism. The excess powder resulting from the spreading process is collected in the collector bin. The remaining powder in the build chamber is exposed to the build conditions such as build chamber temperature, radiant heat, or conductive heat energy [Dingal, 2008] from the laser. It also contains some fused powder ejected from the melt pool area during the build process. It is postulated that such exposure conditions create irregularities in the new layer of powder, affecting the fusion process resulting in variations in as-manufactured material properties. For the purpose of this research, 'recycled' powder refers to the use of powder collected from the build platform and the collector bin. 'Refreshed' powder refers to the use of virgin powder still left in the dispenser bin in addition to recycled powder in a particular build. Recycling of refreshed powder refers to the reuse of powder containing a combination of recycled and virgin powder.

The effect of recycling powder on mechanical properties of built parts is not clear. Some studies indicate that certain powders can be recycled many times without affecting the mechanical properties of the final part [*Jelis et al, 2015*]. Tang et al [*2015*] studied the recycling of titanium alloy powder (Ti-6Al-4V) used in the electron beam melting (EBM) process. They recycled the powder 21 times (21 builds) making six cylindrical tensile samples in each build. They found that tensile properties such as yield strength and ultimate tensile strength increased with powder reuse. They suggest that this is due to an increased oxygen content while the powder is exposed to air. The powder particle size distribution (PSD) became narrower as the result of small particles being removed from the build chamber during clean up, while the 80 ☐m sieving removed larger, agglomerated, partially sintered particles. Improved flowability was observed and attributed to the removal of small particles during clean up, and reduced moisture in the powder after repeatedly exposed to the build chamber vacuum, which is maintained at high temperatures (> 550 °C) to minimize residual stresses.

On the other hand, Sun et al [*2015*] reported comparison of flowability of Ti-6Al-4V after recycling over 30 times with that of virgin powder. Their results indicated a reduction in flowability, measured by the increasing angle of repose (AOR), as recycling increased. They suggested that the loss in flowability is due to the powder containing partially molten and distorted particles. Nandwana et al [*2016*] examined the effects of recycling nickel and titanium alloy (IN 718 and Ti-6Al-4V) powders used in the EBM process on powder characteristics. They made a series of builds designed to use 100 % recycled powder in each build (without the need for adding virgin powder). This design resulted in decreasing build heights so as to not require the introduction of fresh powder during the build series. They detected an increase in the amount of oxygen content most likely from air exposure during handling, but the content was still within specification. They did not find a significant change in powder flowability, morphology, or particle size distribution over their series of builds suggesting that these two powders can be reused many times. Al-Bermani et al [*2010*] recycled Ti-6Al-4V powder, used in the EBM process, over 20 times. However, they found that as the powder was recycled, the oxygen content increased to levels beyond the material specification. They reported that the source of the oxygen is water absorbed into the internal surface of the vacuum chamber and into the titanium powder.

Slotwinski et al [*2014*] performed a series of eight builds with 17-4 stainless steel powder using a laser-based PBF process, recycling the powder after each build. The powder was collected and characterized after various builds. The powder PSD, determined by laser diffraction (LD), increased over the series of builds, especially during Builds #5 through #8, suggesting that smaller particles were being sintered together and being counted by LD as a single, larger, particle. Microstructure of recycled powder was investigated using the quantitative X-ray diffraction (XRD) technique. A slight increase in body centric cubic (BCC) phase with a corresponding slight decrease in face centric cubic (FCC) phase was observed in the powder over the course of eight builds. X-ray computed tomography (XCT) determined no significant change in the length to width ratio of powder particles of samples from Builds #1 to #8, but an unexplained change occurred in the width to thickness ratio of the same powder particles. X-ray photoelectron spectroscopy (XPS) determined no significant change in elemental concentrations from the virgin and recycled powder.

Jelis et al [*2015*] did not find a difference in mechanical (tensile) properties of specimens made with virgin and once-recycled ANSI 4340 steel powder using the laser-based PBF process.

The objective of this study is to determine the effects of recycling of stainless steel (S17-4 PH) powder, used in laser-based PBF process, on the mechanical properties of built parts and powder characteristics. S17-4 PH is a martensitic precipitation-age-hardening stainless steel which conforms to the United States unified numbering system (UNS) classification of S17400 (Type AISI630) according to the ASTM A564 / ASTM A564M [*2013*]. S17-4 PH is generally used for parts which require corrosion resistance and high strength at temperatures up to 315 °C. S17-4 PH in solution-annealed condition is characterized with good machinability, which may be age-hardened to the specified mechanical properties. The main reason for the high corrosion resistance is the high amount of chromium between 15.00 % to 17.00 %, which forms an unreactive passive

layer on the material surface. Due to the predominant body centered tetragonal (BCT) martensitic phase, which primarily forms upon cool down after annealing, S17-4 PH gets harder by the formation of non-coherent face centered cube (FCC) copper- (Cu-) rich precipitants [*Murr et al, 2012*].

To simulate industrial practice in the use of recycled powder, in contrast to the previous studies, in this study a simulated industrial powder management strategy is applied, which is explained in the following section. Mechanical properties of additively manufactured parts were evaluated using tensile and hardness tests. Recycled powder properties, such as particle size distribution (PSD), flowability, chemical composition, and microstructure, are evaluated and compared against that of the virgin powder.

2. Experimental Methodology

Stainless steel (S17-4 PH) powder is used in a laser-based PBF machine. **Table 1** shows the chemical composition of the virgin powder provided by the powder supplier. The S17-4 PH powder was atomized in nitrogen. According to the certification sheet from the powder vendor [*EOS, 2014*] the virgin S17-4 PH powder has a particle size of $D_{96.8} = 53$ µm determined by sieve analysis.

Table 1: Chemical composition of the virgin stainless steel (17-4 PH) powder as reported by the powder supplier.

Element content, [mass percentage]	Chemical composition of the virgin stainless steel S17-4 PH powder, (EOS, mill, S17-4, 2014)
Carbon; C	≤ 0.07
Manganese; Mn	≤ 1.00
Phosphorus; P	-
Sulfur; S	-
Silicon; Si	≤ 1.00
Nickel; Ni	3.00 to 5.00
Chromium, Cr	15.00 to 17.50
Molybdenum; Mo	≤ 0.5
Copper; Cu	3.00 to 5.00
Nitrogen; N	-
Tantalum Ta + Niobium Nb	0.15 to 0.45

A series of 11 builds were completed with varying amounts of virgin and recycled powder following a specific powder recycling strategy, which is explained in the next section. Each build consisted of six tensile specimens and three witness cubes (Figure 1 and Figure 2) deposited on a 25.4 mm thick steel (AISI 1045) build platform, which has an area of 250 mm x 250 mm. Three powder bed density (PBD) capsules were included in builds #1, #5, and #11. The near net shape tensile specimens were located horizontally on the build platform with their longitudinal axes parallel to the direction of the recoating arm motion (x direction) [*ISO/ASTM 52921, 2013*] (**Figure 2**). The tensile specimens were manufactured solidly connected to the build platform along 15 mm length sections on each end. The solid connection helped anchor the specimen ends, preventing warping that could interfere with the recoater arm motion. The remaining middle section of the specimens

have support structures underneath to provide stability and prevent warping due to residual stress.
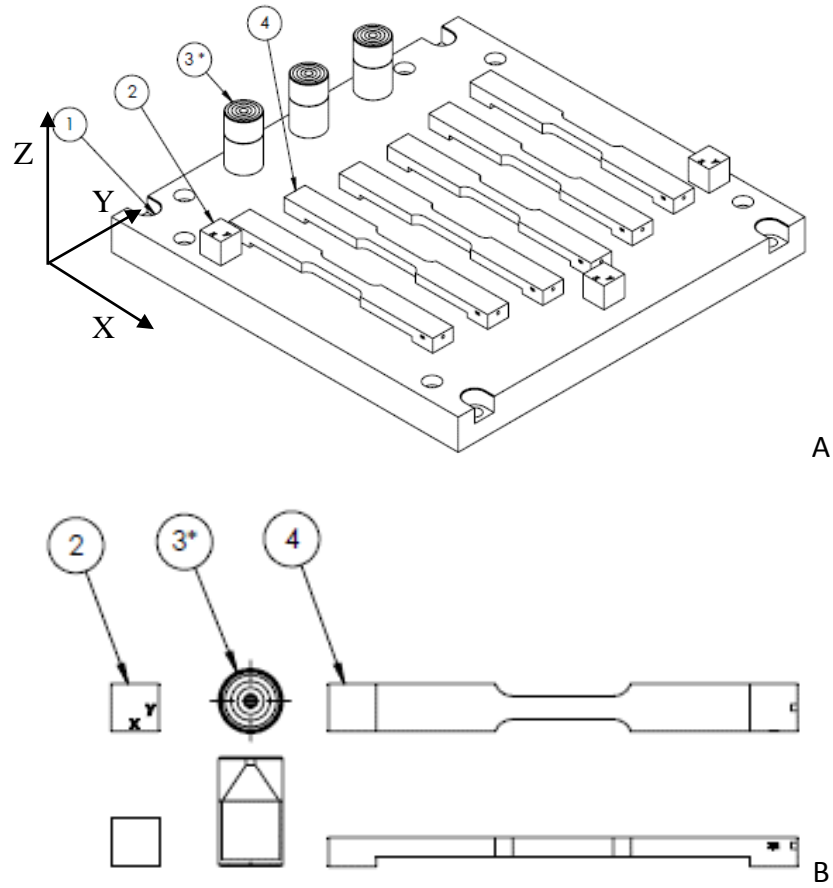
Figure 1: A) Build layout with three test cubes (2), three powder bed density capsules (PBD specimens) (3*) and six net-shape tensile specimens (4) on the build plate. PBD specimens (3*) were only included in Builds #1, #5, and #11. B) Top and side view of the three types of specimens
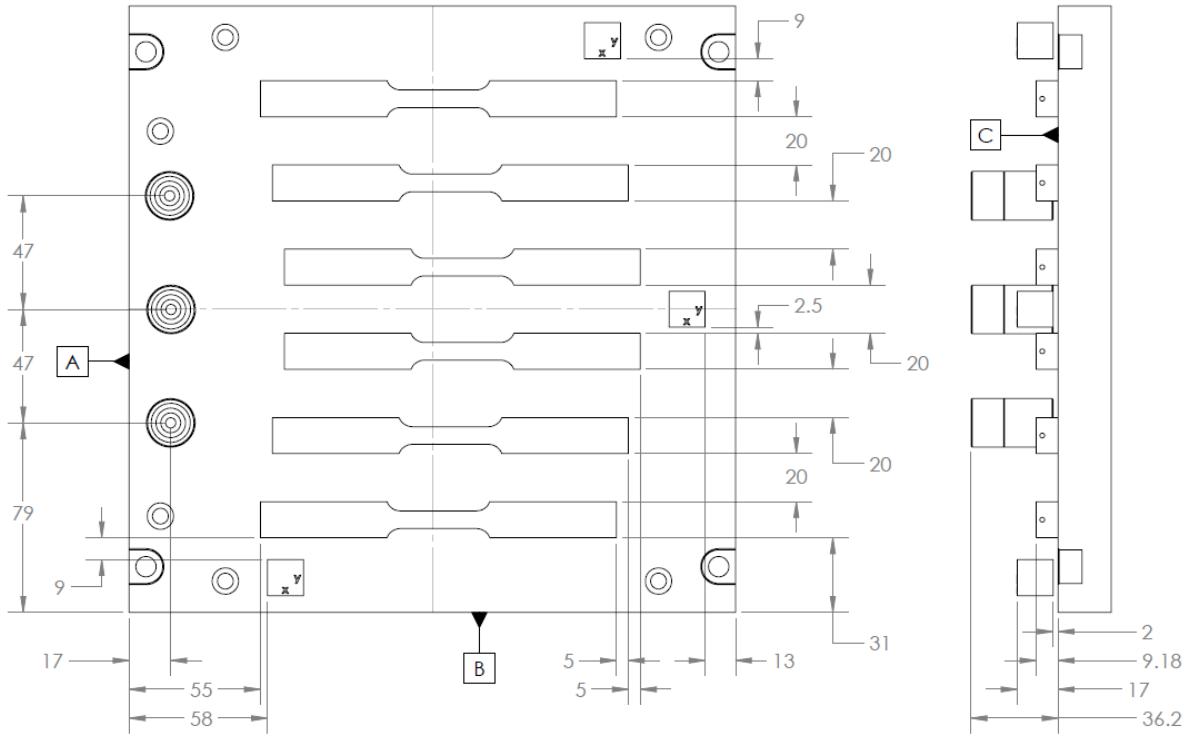
Figure 2: **Specimen arrangement on build platform; layout includes PBD capsules for Builds #1, #5, and #11. Recoater direction parallel to Datum B moving from right to left. Dimensions are in millimeters.**
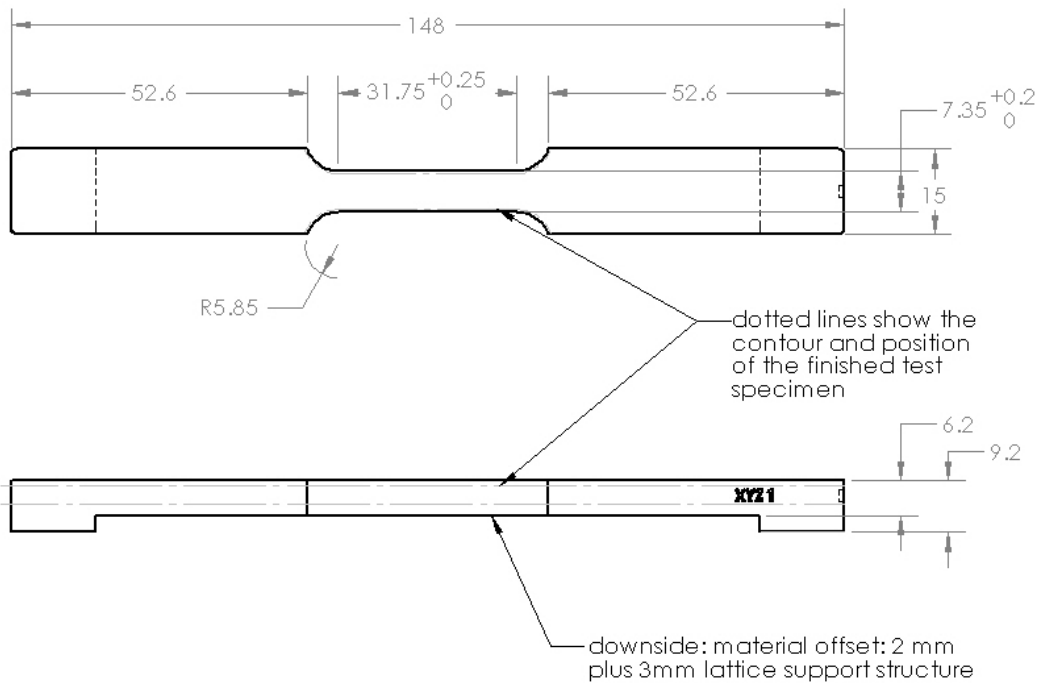
Figure 3: Net-shape tensile specimen. Dimensions are in millimeters.

5

The process parameters used in the build process are shown in Table 2.

Table 2: Nominal machine settings for this study.

Parameter	Skin	UpSkin	Post-Contour
Scan Pattern	Striped	Striped	x
Stripe Width	4 mm	4 mm	x
Laser Power (P_L) [W]	195	160	60
Scan Speed (v_L) [1000 mm $\cdot$ s^{-1}]	1000	500	700
Layer Thickness (t_L) [mm]	0.02	0.02	0.02
Assumed Laser beam diameter (d_L) [mm]	0.1	0.1	0.1
Raster Line Separation / Hatch (h_L) [mm]	0.1	0.1	X
Atmosphere	N_2	N_2	N_2
Volume Rate (VR) [mm$^3 \cdot$ s^{-1}]	2.0	1.0	1.4
Energy Intensity (E_I) [J $\cdot$ mm^{-2}]	1.95	3.2	0.86
Global Energy Density (E_G) [J $\cdot$ mm^{-3}]	97.5	160.0	42.86

2.1.   Build Sequence and Powder Recycling Strategy

Build #1 began with 100% virgin stainless steel powder in the dispenser bin (Figure 4). After Build #1, the powder on the build plate is mixed with the powder in the collector bin. This powder was sieved (80 µm) to remove any oversized particles and defined as 'recycled' powder. The recycled powder is then added to the top of the unused virgin powder remaining in the dispenser bin in preparation for Build #2 (Figure 5). The recycled powder and unused virgin powder are not mixed in the dispenser bin to ensure that the recycled powder from the previous build is used first in the following build (as shown in Figure 6).

The powder in the dispenser bin for Build #3 consisted of recycled powder from Build #2 at the top, powder recycled from Build #1 in the middle, and virgin powder on the bottom (Figure 6). Build #3 was therefore manufactured with 90 % recycled powder from Build #2, and 10 % of recycled powder from Build #1, as is also shown in Figure 7. The virgin powder at the bottom of the dispenser was not used to manufacture Build #3.

To determine the amount of powder used for each build and the amount of recycled powder, the depths of powder in the dispenser bin before and after the build were measured using a ruler. Table 3 shows the composition of the dispenser bin with the measured amounts of virgin and recycled powder for each build.
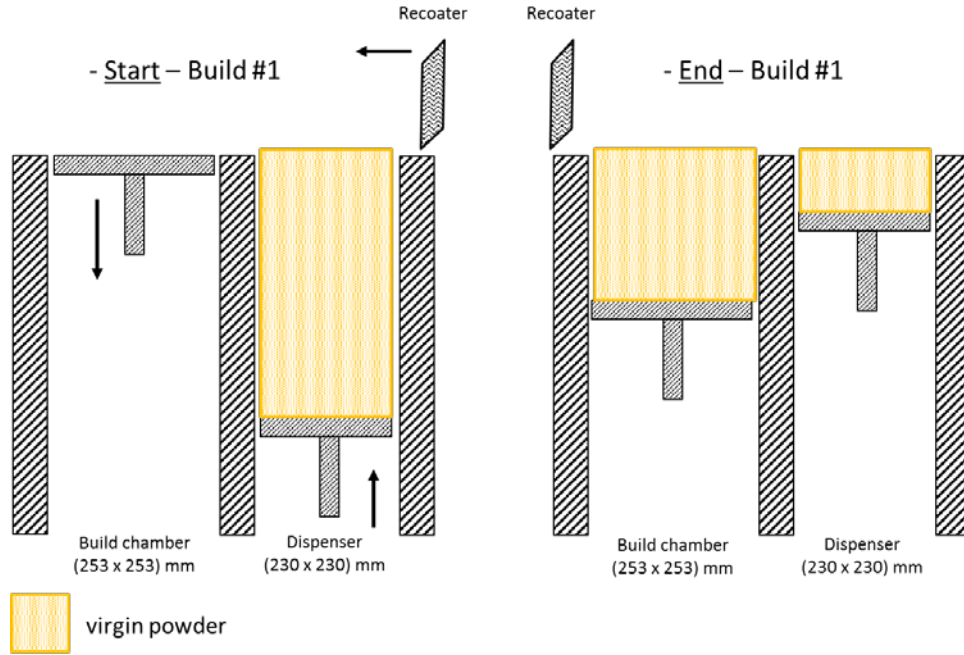
Figure 4: Build #1 start and ending powder conditions, 100% of the powder in the dispenser was virgin powder at the start of Build #1.
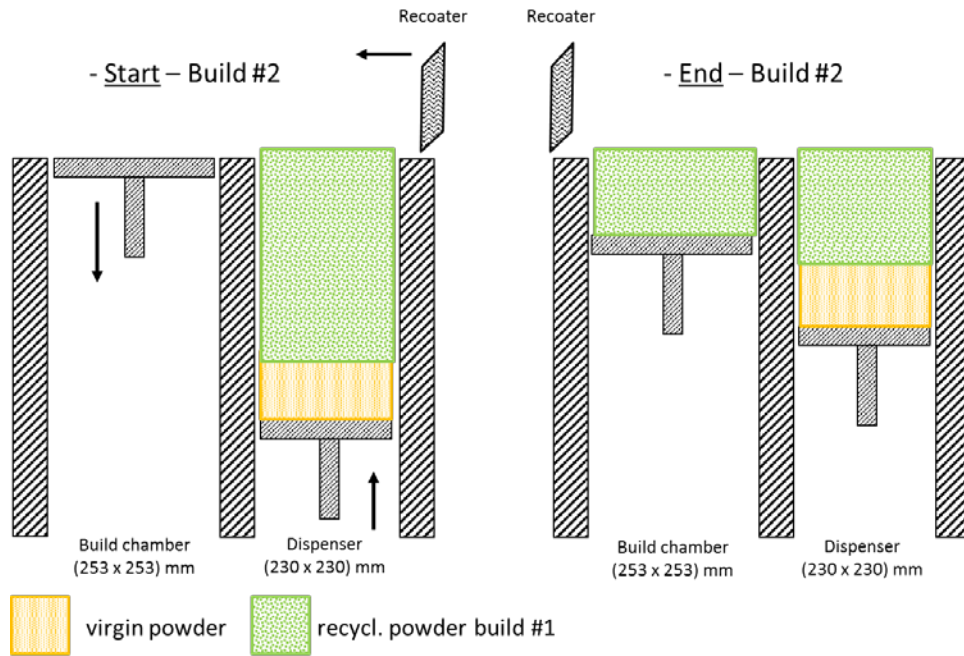
Figure 5: Build #2 start and ending powder conditions, 100% of the powder used to manufacture Build #2 was recycled powder from Build #1.
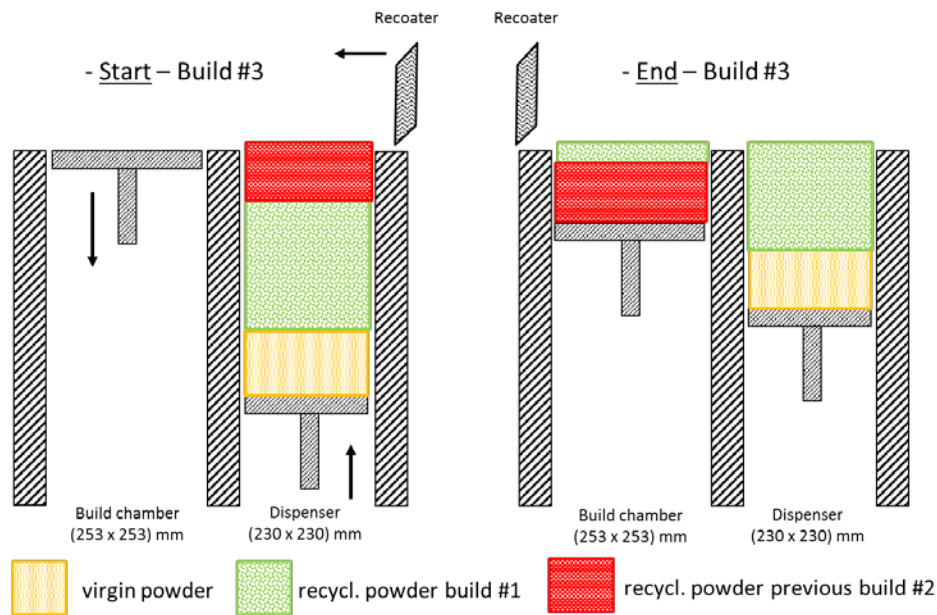
Figure 6: Build #3 start and ending powder conditions, 90 % of the powder used to manufacture Build #3 was recycled powder from Build #2 and 10 % from Build #1.

Table 3: Measured powder depth in dispenser bin and determined amount of powder for build.

Build	Build type	Depth of powder before build [mm]	Depth of powder after build [mm]	Used powder [mm]	Recycled powder amount for the next build [mm]
1	With PBD	182	79.4	102.6	90.1
#2	No PBD	169.5	125.4	44.1	40.3
#3	No PBD	165.7	120.7	45	37.6
#4	No PBD	158.3	115.9	42.4	40.6
#5	With PBD	156.5	55.6	100.9	93.8
#6	No PBD	149.4	104.8	44.6	40.2
#7	No PBD	145	100	45	41.9
#8	No PBD	141.7	95.2	46.5	40
#9	No PBD	135.5	92	43.5	39.7
#10	No PBD	131.8	85.7	46.1	41.3
#11	With PBD	126.9	35	91.9	

Since there were two build types, builds with and without PBD capsules, the total build heights were different: 36.2 mm for builds with PBD capsules (Build #1, #5, #11) and 17

8

mm for the other builds. Therefore, different amounts of powder were required to manufacture these two build volumes.

Based on the powder amount and composition in the dispenser bin before each build, the composition of each completed build was determined (Figure 7). At least 40 % of each build, including the tensile bars, consisted of powder recycled from the previous build. Beginning with Build #3, the witness cubes were always made out of two different recycled portions. Most of the solid material with approximately 13 mm along the build direction was made of the recycled powder from the previous build, and the last (approximate) 2 mm of layers on top were made of the recycled powder from Build #1. Likewise, beginning with Build #7, the top 2 mm layers of each build was manufactured from the recycled powder from Build #5. It should be noted that, as shown in Figure 7, Build # 5 uses a fraction of virgin powder (about 23%), that is still left in the dispenser bin during the previous builds; therefore, after Build #5, all recycled powders are "*refreshed*" (virgin powder was mixed with other recycled powder during sieving), which is noted as "recycled*".
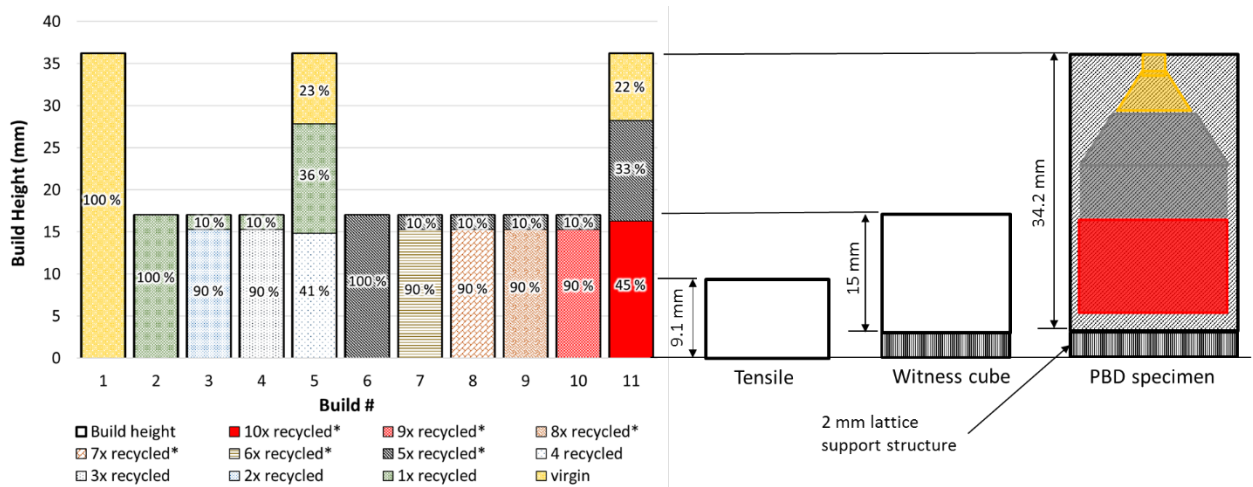
Figure 7: Percentages of powder portions for each build in comparison to the different specimen heights

2.2. Post Processing

The completed build plates were wrapped in stainless steel bags and heat treated for stress relief in an oven in an argon environment at 650 °C and held for 1 hour, after taking 6 hours to reach this target temperature. The build platform was allowed to cool in the oven for 15 hours before being removed to continue cooling to room temperature. The exception to this process was for the build plates that included PBD capsules. The capsules were removed using wire electrical discharge machining (EDM) before the heat treatment to prevent the powder within the cylinders from sintering.

After heat treatment, 1 mm was milled off from the top surface over the total specimen length of all tensile specimens while still attached to the build plate. Wire EDM was used to separate the test cubes from the build platform. Wire EDM was also used to separate the near-net-shape tensile specimens from the build platform. An additional 0.5 mm was milled from the side faces of the gauge section. Grinding was used to obtain the final

9

specimen thickness of 3.175 mm. The final tensile specimen geometry conforms to ASTM E8/E8M [*2013*] (Figure 8).
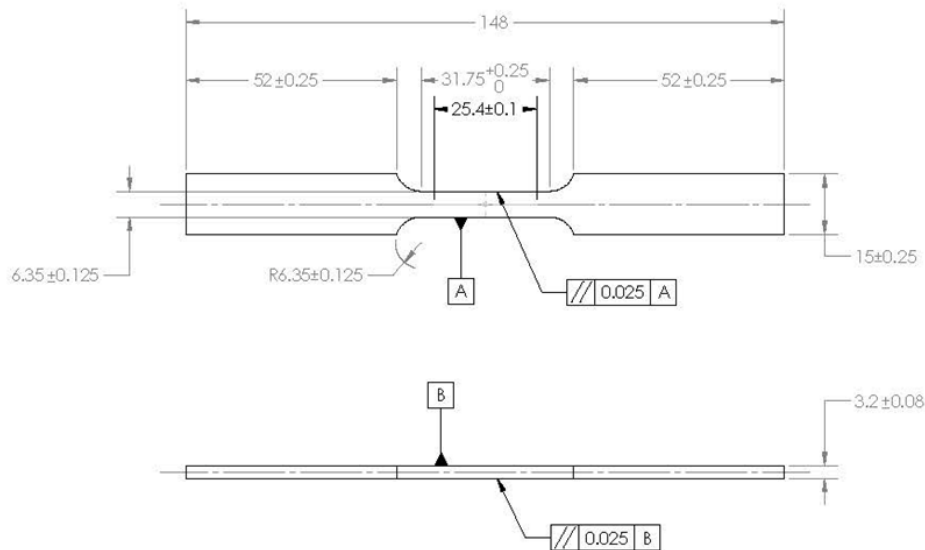
Figure 8: Final tensile specimen geometry according to ASTM E8/E8M. Dimensions are in millimeters.

2.3.   Tests conducted

Recycled powder properties were assessed in terms of morphology, chemistry, microstructure, particle size distribution, and powder bed density.   To characterize additively manufactured material properties, tensile specimens and witness cubes were used to determine tensile strength, hardness, surface roughness, bulk density, chemistry, and microstructure. These tests are described below.

2.3.1.   Powder morphology, particle size distribution, microstructure, and chemistry

Powder samples were taken at various times during the build sequence for analysis. The first powder sample (120 g) was taken from within the laser-based PBF machine dispenser bin prior to starting a build. After each build, the second powder sample (20 g) was taken from inside the build chamber close to the surface of the build, and a third sample from the middle of the powder bed (20 g). A fourth powder sample (20 g) was taken from the collector bin after each build.

Using a scanning electron microscope (SEM), secondary electron images of sampled powders, packed in a 2 mm deep cavity mount, at two magnifications were collected to show overall and detailed powder morphological characteristics for the samples.

A dynamic image analysis system was also used to characterize the morphology of the powder samples and the powder size and shape distribution according to ISO 13322-2 [*2006*]. The instrument captures dispersed powder particle shadows using two digital cameras with different magnifications while a software program measures and determines

the particle sizes and shape distribution. For this study, we used the dynamic imaging system to describe the powder morphology by calculating the aspect ratio (a_3) of powder particle images.

To characterize the crystal structures of the powders, X-ray diffraction patterns were obtained from the samples in the cavity mounts. An approximate interaction depth for X-ray radiation for stainless steel is approximately 2 μm, making these analyses very sensitive to the surface condition of the metal particles. The low interaction depth may provide an advantage where changes in the surface characteristics need to be detected.

2.3.2. Powder apparent density and flow rate

Powder sampled from the dispenser bin was used to determine the apparent density following ASTM B212 [*2013*], and used to determine the flow rate following ASTM B213 [*2013*]. Both methods use the Hall Flowmeter Funnel.

2.3.3. Powder bed density

Three powder bed density (PBD) cylinders were included on the build platform of Builds # 1, # 5, and # 11 (**Figure 9**). The PBD cylinders capture the powder density inside the build chamber directly on the build platform during the manufacturing process [*Jacob et al, 2016*]. The mass of the powder removed from the interior volume is measured to calculate the powder density.
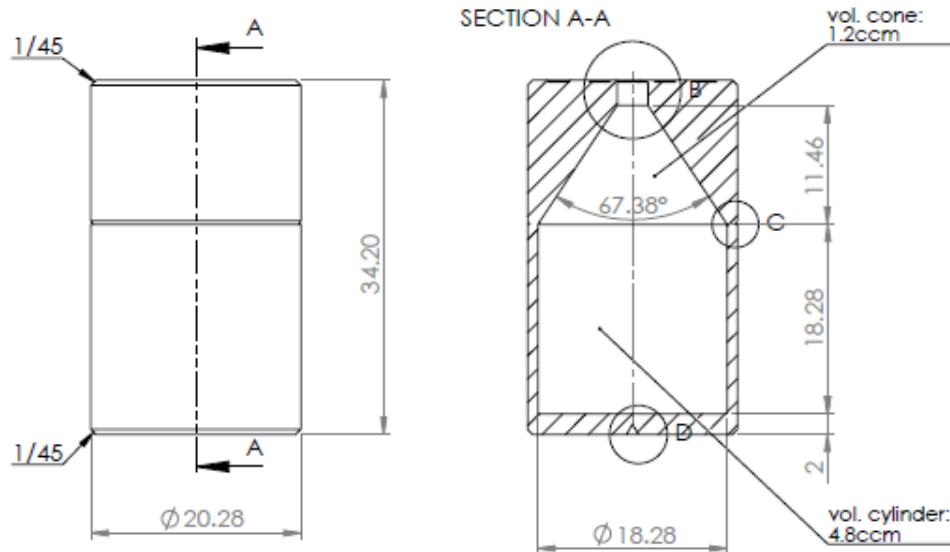
Figure 9: Powder bed density capsules are used to determine the powder bed density directly on the build platform during the manufacturing process, dimensions in millimeters except volume in cubic centimeters (ccm).

2.3.4. Tensile properties of manufactured specimens

Tensile properties of specimens (see Figure 8) like the ultimate tensile strength (UTS), the elastic modulus (E), the 0.2 % offset yield strength (YS), and the upper yield strength (UYS), were measured according to the ASTM E8/E8M [*2013*]. The tensile specimens are placed in a tensile testing machine and tested until failure under displacement control.

11

An extensometer was attached to the gauge section during the initial loading at a nominal strain rate of 0.015 mm/mm/min to determine the YS and UYS based on the extensometer signal. Once the specimen was loaded past yielding, the extensometer was removed and the test continued until failure at a nominal strain rate of 0.05 mm/mm/min. Elongation (A) was measured by carefully putting the tensile ends back together after fracture and measuring the elongation of the 25.4 mm gauge section.

2.3.5. Dynamic elastic modulus

Material properties, such as Young's Modulus, Shear Modulus, and Poission's Ratio, of manufactured specimens were determined using the impulse excitation method by applying longitudinal and transverse ultrasonic waves to a material surface and measuring the time difference between the sent and received signals [*ASTM E1876, 2015*]. Young's Modulus (Y) was determined along two directions on the tab ends of the tensile specimens: along the build (vertical) direction (z axis) across the thickness of 3.175 mm and along the horizontal direction (y axis) across the tab width of 12 mm.

2.3.6. Hardness, surface roughness, and bulk density of manufactured test cubes

Each build included three witness cubes, which were used for hardness, surface roughness, and density measurements. The surface roughness of the top surface (xy- plane) and the side surface (xz- plane) of each cube was measured using white light interferometry. The bulk density of the cubes was measured using the Archimedes technique submerging the cubes in water and determining the density from the water displacement. The hardness of the cubes was determined on the ground top surface on the xz- plane, after 1 mm height of the material was removed from the top, using a Rockwell hardness tester (HRC scale).

2.3.7. Chemistry and microstructure of manufactured specimens

Specimens extracted from the stress-relief-heat-treated and as-manufactured witness cubes, parallel to the build direction, were ground and polished using standard metallography procedures. To reveal the microstructure, the samples were etched using Swede's etchant (50 mL H_2O + 5 mL HCl + 5 mL HNO_3 + 6 g $FeCl_3$). Microstructural and micro chemical analyses were carried out using scanning electron microscopy with a silicon drift detector for energy dispersive spectroscopy (EDS). During the analysis operating voltage and current were set as 15 kV and 1.5 nA, respectively. Material phase identification was measured by using an X-ray diffractometer by applying copper (Cu) Kα radiation at an operating voltage of 45 kV, and current of 40 mA. X-ray diffraction patterns were obtained within a Bragg angle (2Θ degrees) range of 20° to 100° at increments of 0.05° with the counting time of 1 s per increment. The two steel phases of BCC ferrite and BCT martensite have a very small difference in their tetragonality, and therefore not distinguishable with the available equipment for the XRD analysis. Hence, the intensity peaks for BCC phases were simply referred as ferrite-martensite. Furthermore, chemical analysis of witness cubes was conducted by a commercial service laboratory following standard procedures identified in ASTM E1019 [*2011*] and ASTM E1086 [*2014*].

3. Results and Discussion

3.1. Analysis of powder properties

In order to determine the effects of recycling on the various powder properties, a select number of powder samples from different builds and different locations were studied. The list of these powder samples and their associated labels are given in Table 4.

Table 4: Analyzed powder samples

Powder Sample #	Build #	Before/After Build	Sampled Location	Powder Condition
P-40	1	before	Dispenser bin	virgin
P-41	1	after	Build platform, middle	exposed (unsieved)
P-42	1	after	Build platform, close to solidified part surface	exposed (unsieved)
P-43	1	after	Collector bin	exposed (unsieved)
P-44	1	after	PBD capsules	exposed (unsieved)
P-46	2	before	Dispenser bin	recycled once
P-61	5	before	Dispenser bin	mixture of virgin and four times recycled powders
P-65	5	after	PBD capsules	mixture of recycled and virgin (unsieved)
P-67	6	before	Dispenser bin	refreshed, mixed, and recycled
P-92	11	before	Dispenser bin	mixture of recycled powders
P-96	11	after	PBD capsules	mixture of recycled and virgin (unsieved)
P-98	11	after	Dispenser bin	mixture of recycled powders, Represents final state of the powder after the 11 build series.

3.1.1. Powder Morphology

Images from samples obtained by white light stereo microscope (SM) were used to visually assess the effects of powder conditions on the particle size, morphology, and tendency to join with other particles. Figure 10 and Figure 11 show images of the virgin powder (P-40) before the Build #1 and the recycled powder after the last Build #11 (P-98), spread on a sample holder.

13
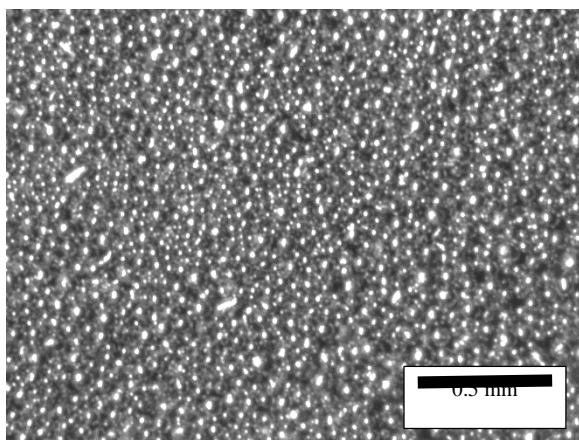
Figure 10: SM (white light) image of sample P-40, VIRGIN S17-4 PH powder before Build #1, dispenser bin
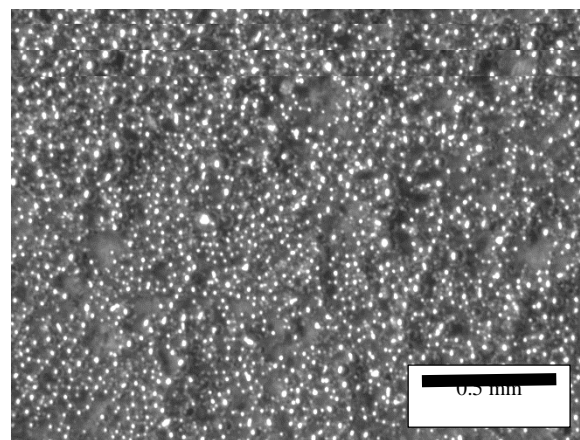
Figure 11: SM (white light) image of sample P-98, RECYCLED S17-4 PH powder after Build #11, dispenser bin

Both powder samples appear similar in color and texture. However, it appears that there are a relatively higher number of large size particles in the virgin sample. Furthermore, some level of clumping is also observed in the recycled powder (sample P-98).

Secondary electron (SE) images of powder morphology at two magnifications were collected, using a scanning electron microscope (SEM), to show overall and detailed powder morphological characteristics for the selected powder samples given in Table 4 (Figure 12 to Figure 22).

A

B
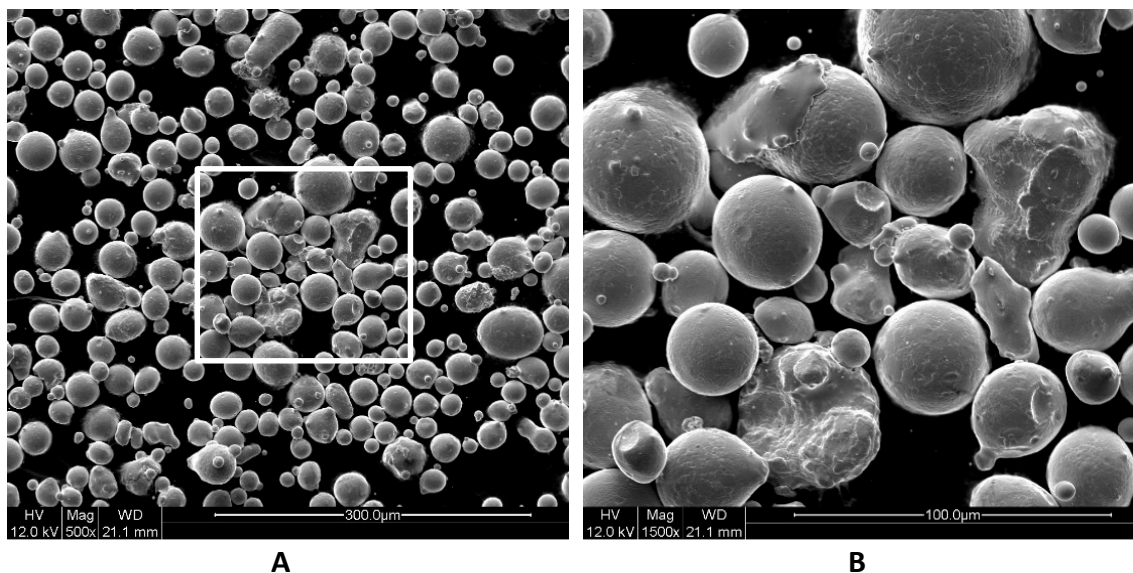
Figure 12: SEM images of sample P-40, VIRGIN, S17-4 PH powder, before Build #1, dispenser bin, lower magnification (A) and higher magnification (B) indicated by the box in (A).

14

A   B
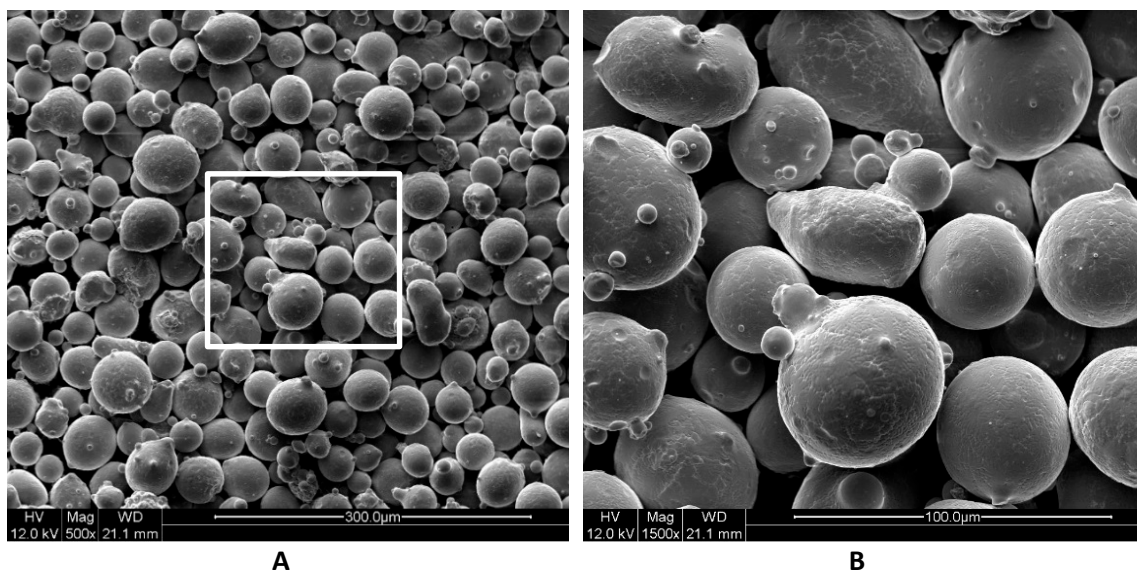
Figure 13: SEM images of sample P-42, RECYCLED, S17-4 PH powder, after Build #1, Build Plate - close to part, lower magnification (A) and higher magnification (B) indicated by the box in (A).

A   B
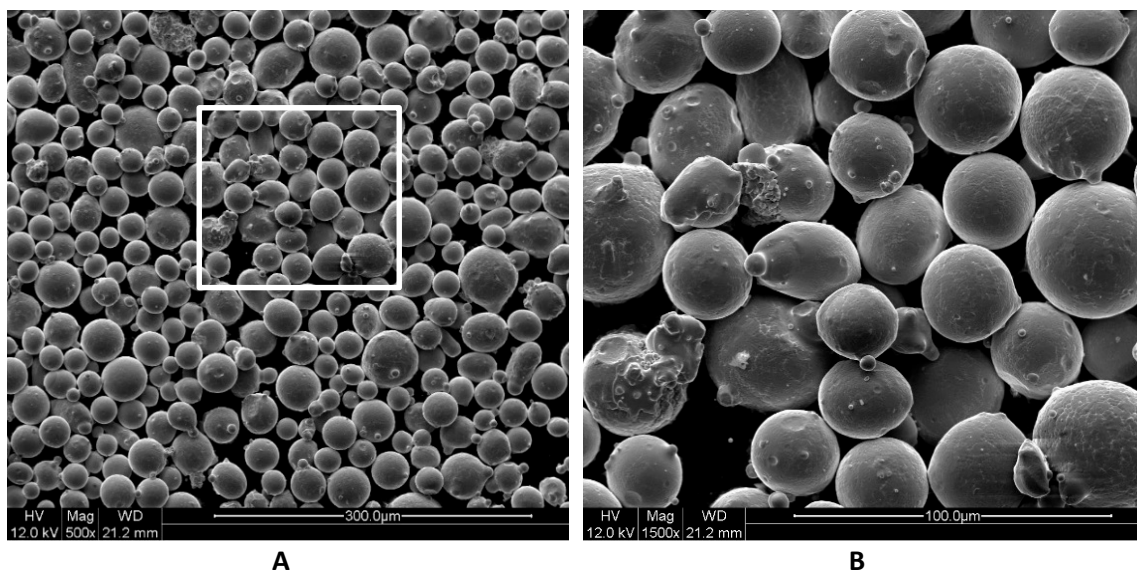
Figure 14: SEM images of sample P-44, RECYCLED, S17-4 PH powder, after Build #1, PBD-sample, lower magnification (A) and higher magnification (B) indicated by the box in (A).

A

B
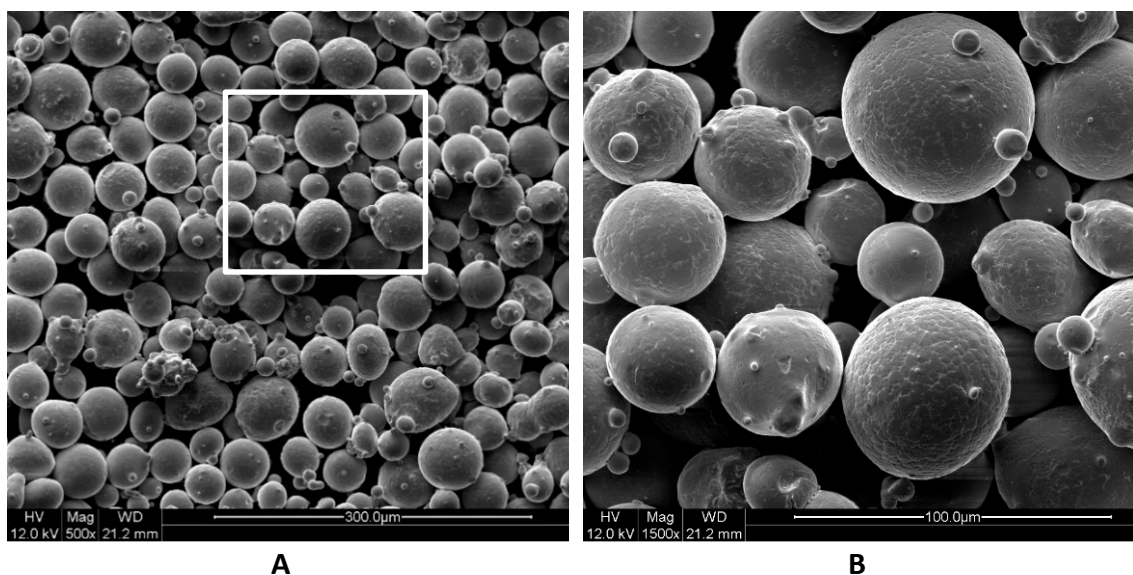
Figure 15: SEM images of sample P-43, RECYCLED, S17-4 PH powder, after Build #1, collector bin, lower magnification (A) and higher magnification (B) indicated by the box in (A).

A

B
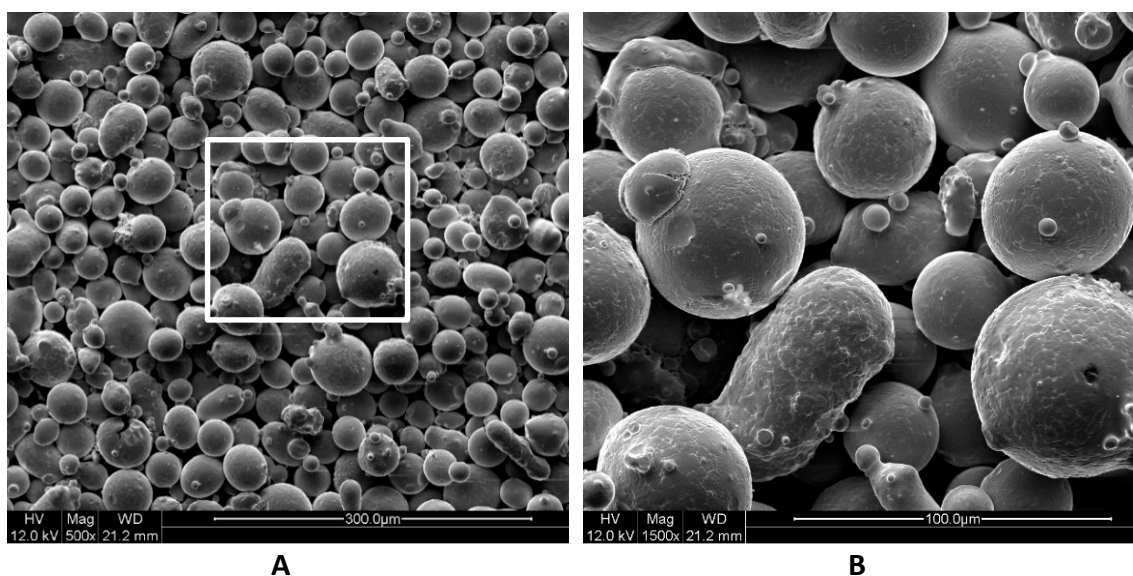
Figure 16: SEM images of sample P-46, RECYCLED, S17-4 PH powder, before Build #2, dispenser bin, lower magnification (A) and higher magnification (B) indicated by the box in (A).

Based on the Figure 11 to Figure 16, the morphology does not change during Build #1. It appears, however, that there are more joined small particles, satellite particles, in the collector bin, along with a higher percentage of larger size particles.

There were no observable differences between the dispenser bin powder from Build #2 (Figure 16, P-46), and the dispenser bin powder from Build #1 (Figure 12, P-40).

There were no observable differences between powders from the PBD capsules (Figure 18, P-65) and from the dispenser bin (Figure 17, P-61) for Build #5.

A

B
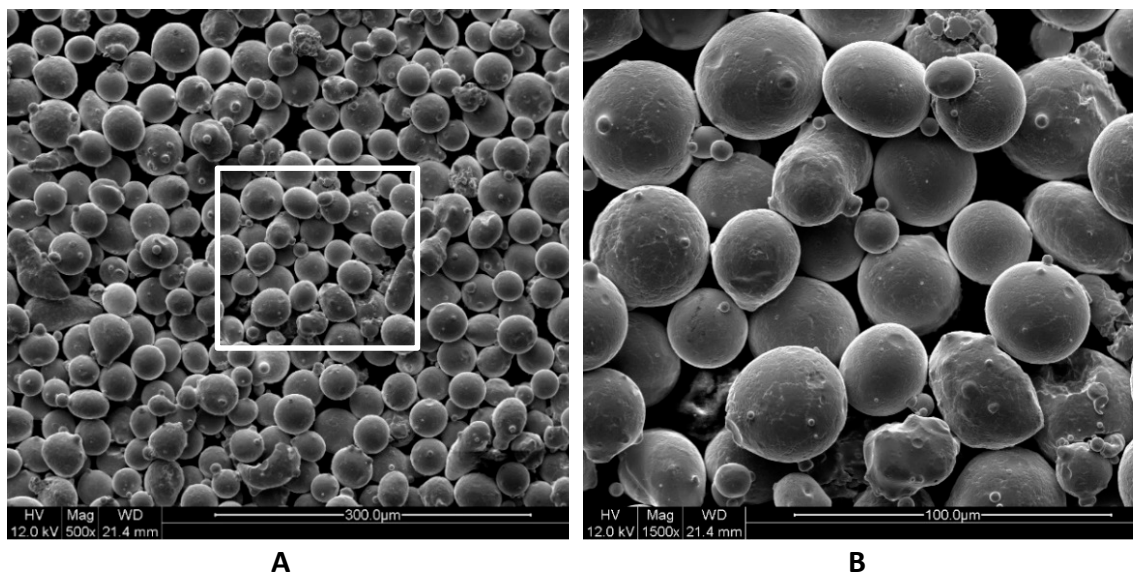
Figure 17: SEM images of sample P-61, RECYCLED, S17-4 PH powder, before Build #5, dispenser bin, lower magnification (A) and higher magnification (B) indicated by the box in (A).

A

B
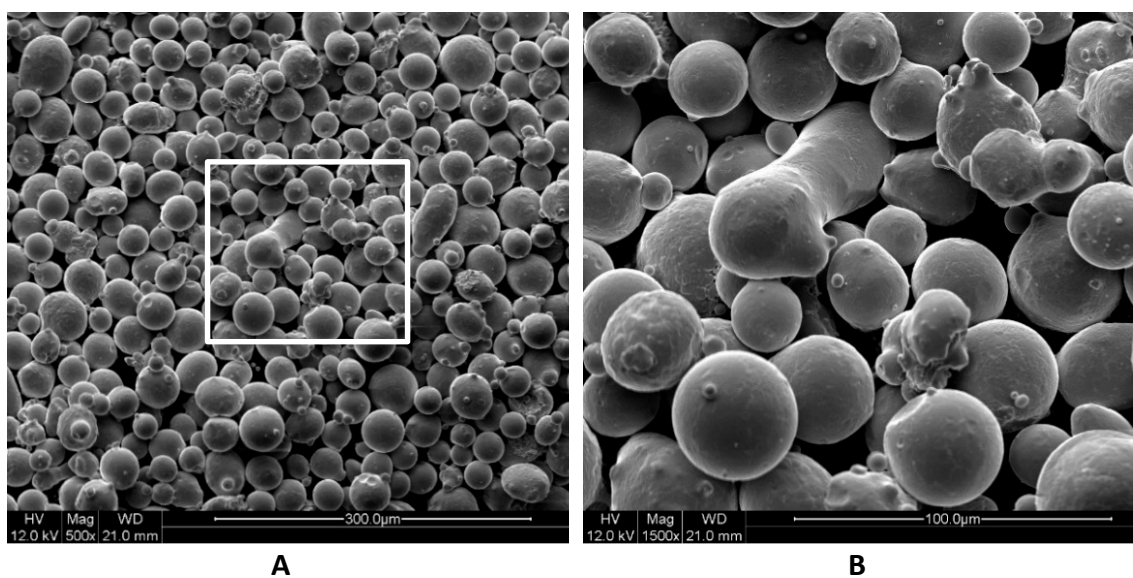
Figure 18: SEM images of sample P-65, RECYCLED, S17-4 PH powder, after Build #5, PBD sample, lower magnification (A) and higher magnification (B) indicated by the box in (A).

A

B
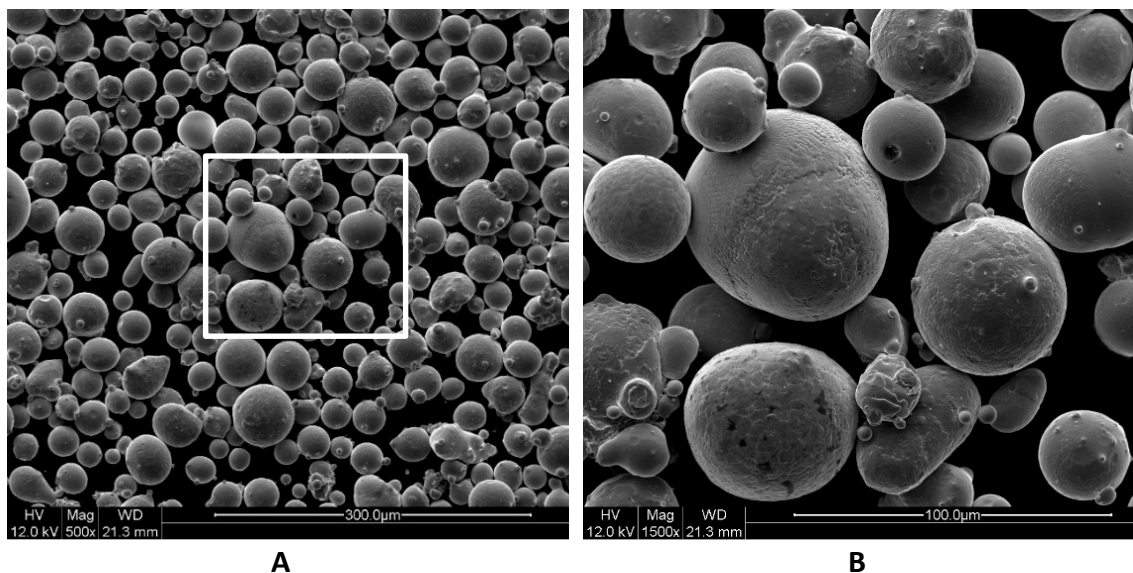
Figure 19: SEM images of sample P-67, RECYCLED, S17-4 PH powder, before build #6, dispenser bin, lower magnification (A) and higher magnification (B) indicated by the box in (A).

A

B
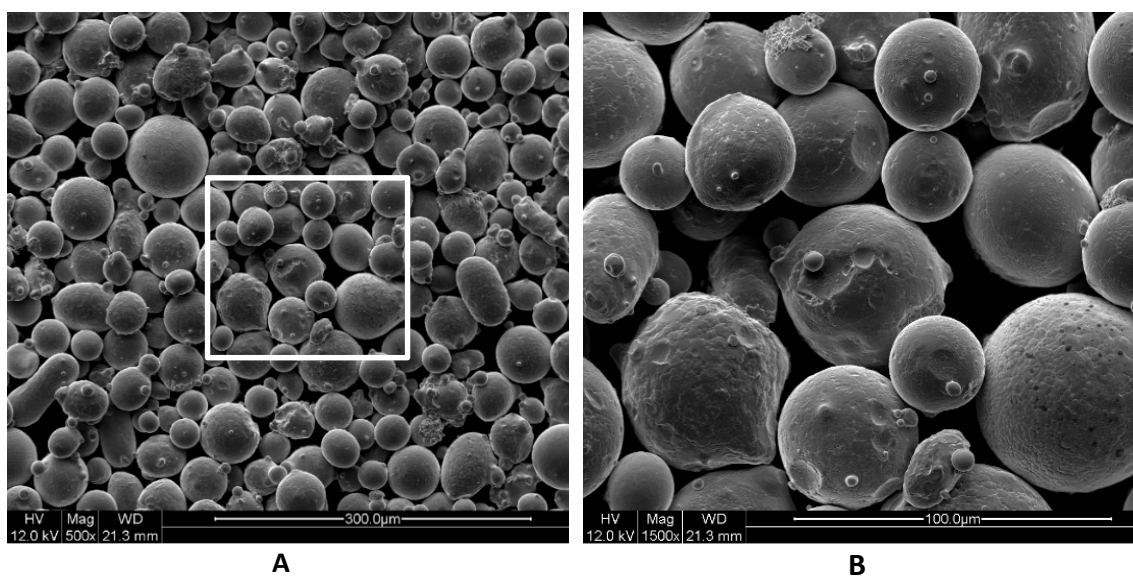
Figure 20: SEM images of sample P-92, RECYCLED, S17-4 PH powder, before Build #11, dispenser bin, lower magnification (A) and higher magnification (B) indicated by the box in (A).

A

B
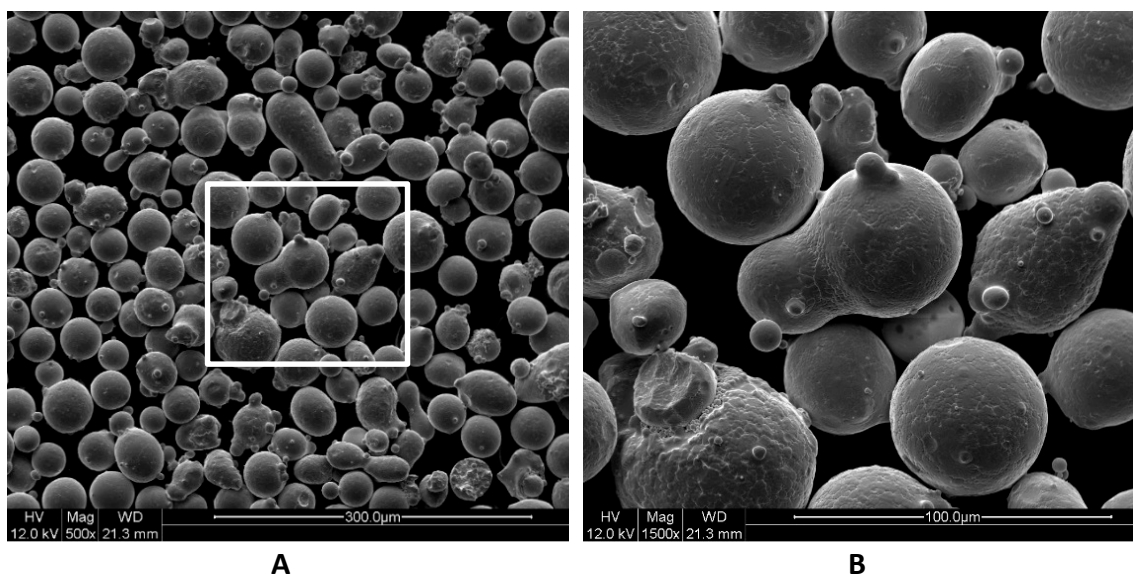
Figure 21: SEM images of sample P-96, RECYCLED, S17-4 PH powder, after Build #11, PBD sample, lower magnification (A) and higher magnification (B) indicated by the box in (A).

A

B
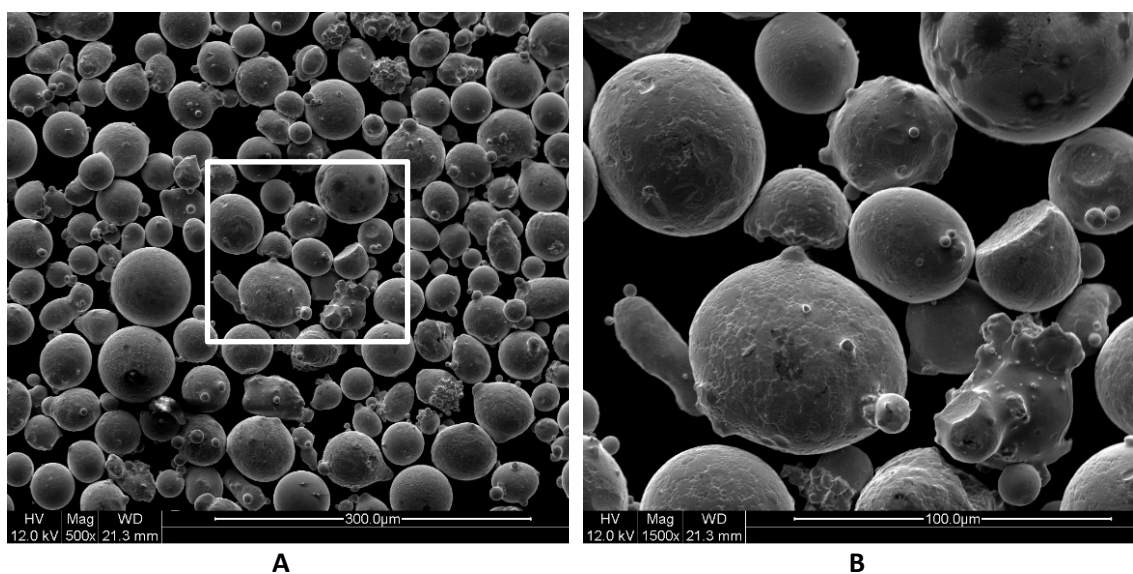
Figure 22: SEM image of sample P-98, Recycled, S17-4 PH powder, after Build #11, dispenser bin, lower magnification (A) and higher magnification (B) indicated by the box in (A).

The overall observation based on SEM images, as presented in Figure 12 to Figure 22, is that powder morphology does not appear to change significantly if recycled up to ten times.

Powder sample morphology was also analyzed using the dynamic digital imaging system to determine the aspect ratios of observed powder particles. Figure 23 shows the principal determination of the Feret diameters (Fe) on the particle projection [ISO 9276-1, 2012]. The aspect ratio (a_3) is the ratio of the width (Fe_{min}) over the length (Fe_{max}) of the particle projection. Fe_{min} and Fe_{max} are determined by the imaging system after multiple projections are made from different directions.

19
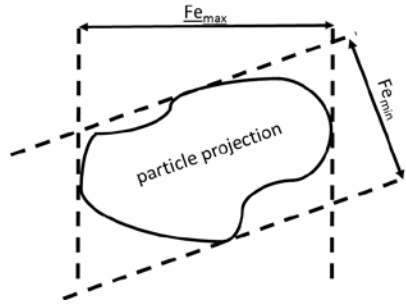
Figure 23: Fe$_{min}$ and Fe$_{max}$ on particle projection

Figure 24 shows the comparison of aspect ratios as a function of particle size for four selected samples (Build #1; P-40, Build #5; P-61, Build #11: P-92, and after Build #11; P-98). The aspect ratios for all three samples is close to 0.85, up to particle size of approximately 50 µm, which corresponds to a nearly spherical shape. However, for particle sizes larger than 50 µm, the aspect ratios vary significantly. To investigate the reason for this variation, a repeatability test is conducted using one powder sample (P-98) and measuring the aspect ratios six times consecutively. The results of this repeatability test (Figure 25) indicate that there is a significant level of variation in determining the aspect ratio for large particle sizes. Since large particles are mostly due to joining of small particles, they exhibit irregular morphology, therefore, the aspect ratio is highly affected by the observation angle. Consequently, values corresponding to particle sizes greater than 50 µm are considered to be unreliable and neglected in this analysis. With these conditions, we conclude that the data do not indicate any significant morphological change in the powder as a result of recycling over eleven builds. This result is consistent with the observation reached using SEM images as shown before.
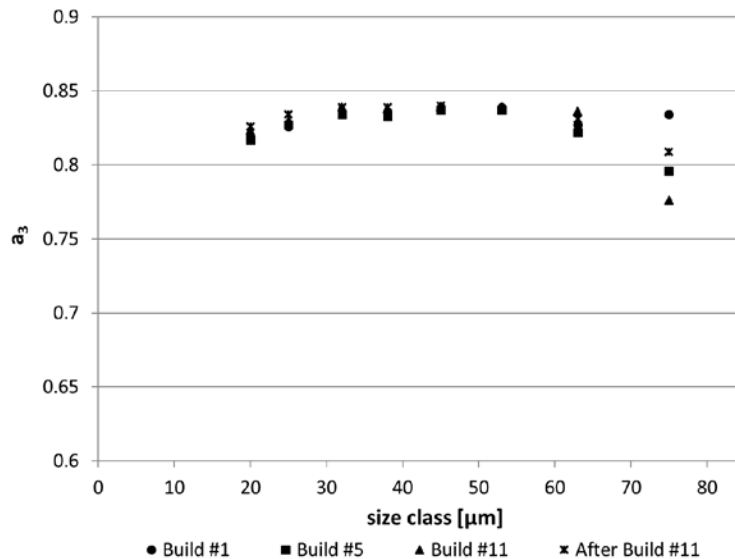
Figure 24: Aspect ratio (a$_3$) versus size class for powder samples from the dispenser bin before the build started. a$_3$ ratio of '1' is a sphere.

20
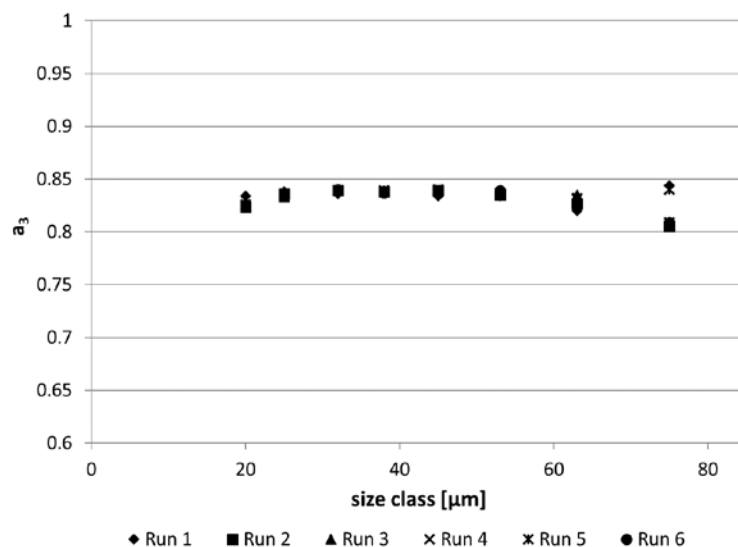
Figure 25: Aspect ratio (a_3) versus size class for 6 runs for the same powder sample showing variability for the larger powder sizes. a_3 ratio of '1' is a sphere.

3.1.2. Particle size and particle size distribution

Dynamic image analysis was used to characterize a subset of powder samples in Table 4. Figure 26 shows the variability in particle size distribution (D_{10}, D_{50}, and D_{90}) for three subsamples taken from the same virgin powder (P-40). Each subsample was analyzed in the instrument six times. The minimum cord diameter (x_{cmin}) was chosen to represent particle size because it measures the minimum width of a particle and it is comparable to results obtained by sieving [*ISO 9276-1, 2012*]. As shown in Figure 26, there is approximately a 2 µm to 5 µm variation of the size distribution for the same powder. The particle size distribution of the S17-4 PH powder according the vendor specification with $D_{96.8} = 53$ µm [*EOS, 2014*] is confirmed with the results of the dynamic image analysis with a determined $D_{90} = 46.3$ µm to 51.2 µm.

Figure 27 shows the particle sizes corresponding to D_{10}, D_{50}, and D_{90} distributions for several powder samples used in this study. Figure 27 shows that the powder size did not change significantly throughout ten recycles.
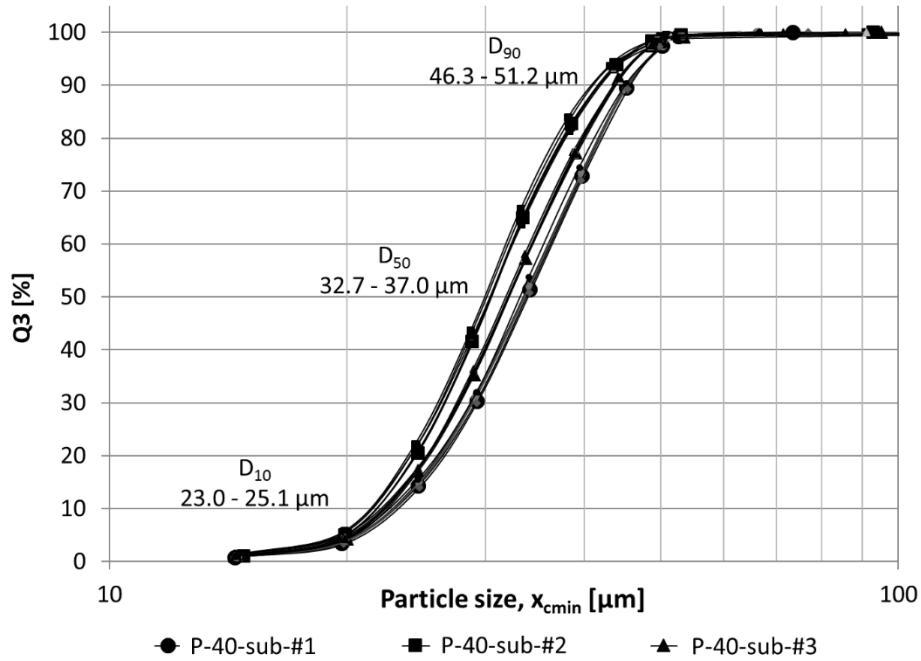
Figure 26: Cumulative particle size distribution (Q₃) of virgin stainless steel S17-4PH powder sample P-40, Build #1 from dispenser bin measured on three subsamples (#1, #2, #3).
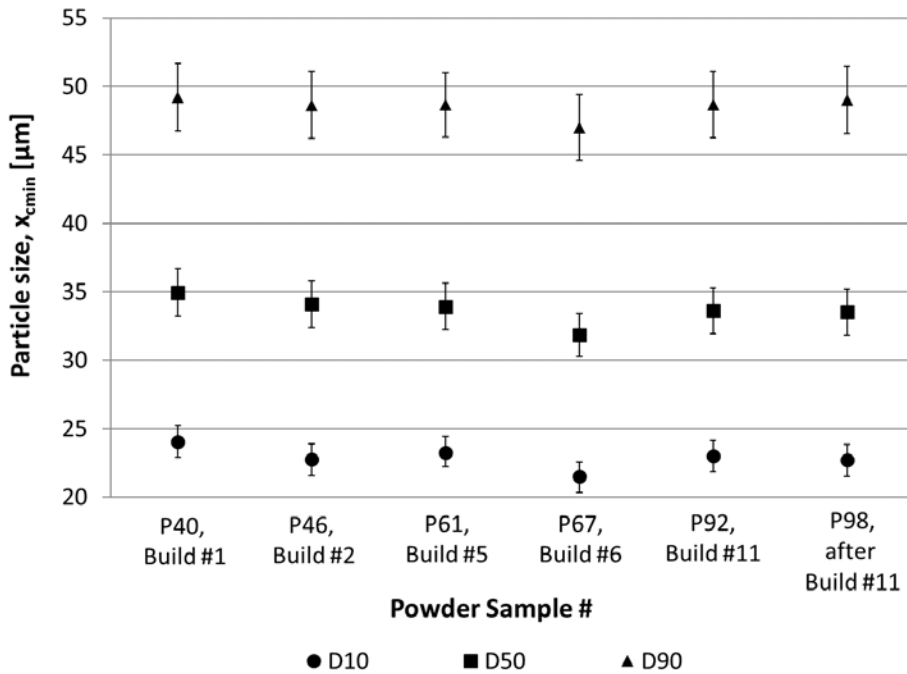
Figure 27: Particle size of Builds #1, #2, #5, #6, #11, and after #11, powder samples with averages of D10, D50, and D90 (Average ± 5 % standard measurement uncertainty) of particle size.

The powder samples contained within the PBD capsules on Builds #1, #5, and #11 (P-44, P-65, P-96) were also analyzed. These powder samples represent the powder that was used to form the powder bed on the build plate after the recoater arm swept across the build platform spreading powder from the dispenser bin. It is assumed that these powder samples represent the particle size distribution of the powder, what is most likely being used to form the powder layer. Figure 28 and Figure 29 show the average of six repeated particle size measurements for each build. A slight decrease appears in powder size comparing the powder samples from the dispenser bin and from the PBD capsules between Builds #1, Build #5, and Build #11. It seems that the powder in the powder bed on the build platform is significantly finer than the powder from the dispenser bin in all three builds #1, #5, and #11, where the PBD capsules were included. Figure 29 shows the standard measurement uncertainty of ± 5 % around the averaged values for D_{10}, D_{50}, and D_{90}. It should be noted, that while P-44 consists of 100 % virgin powder, the other samples contain only approximately 25% of virgin powder. It is assumed that the collector bin may contain some swept particles, which are larger than the clearance between the recoating arm blade and the previously solidified layer.
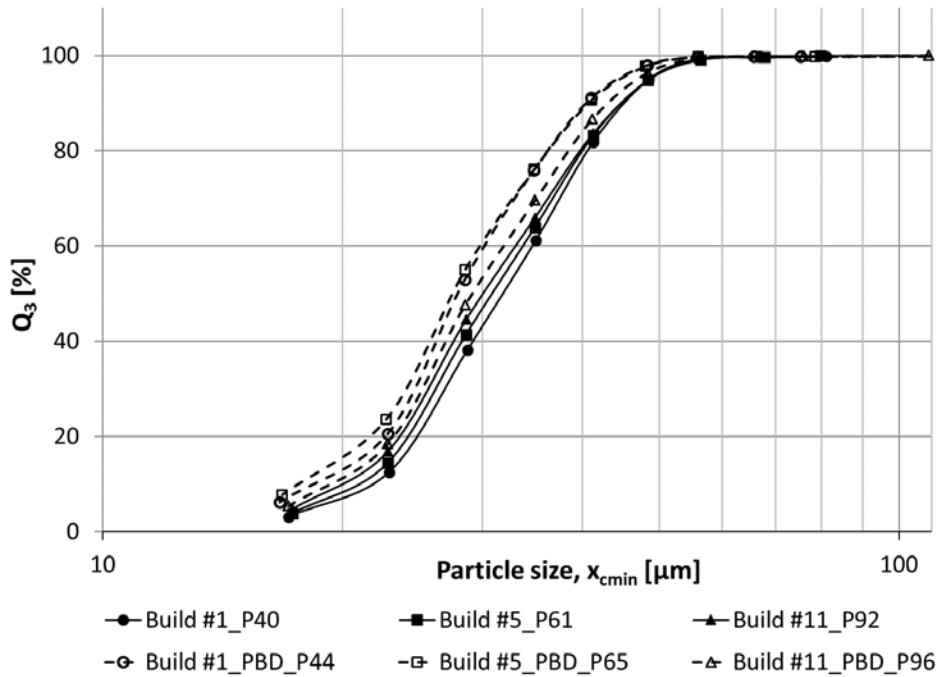
Figure 28: Comparison of cumulative particle size distribution (Q3) between powder from the dispenser bin and PBD specimens for Builds #1, #5, and #11.
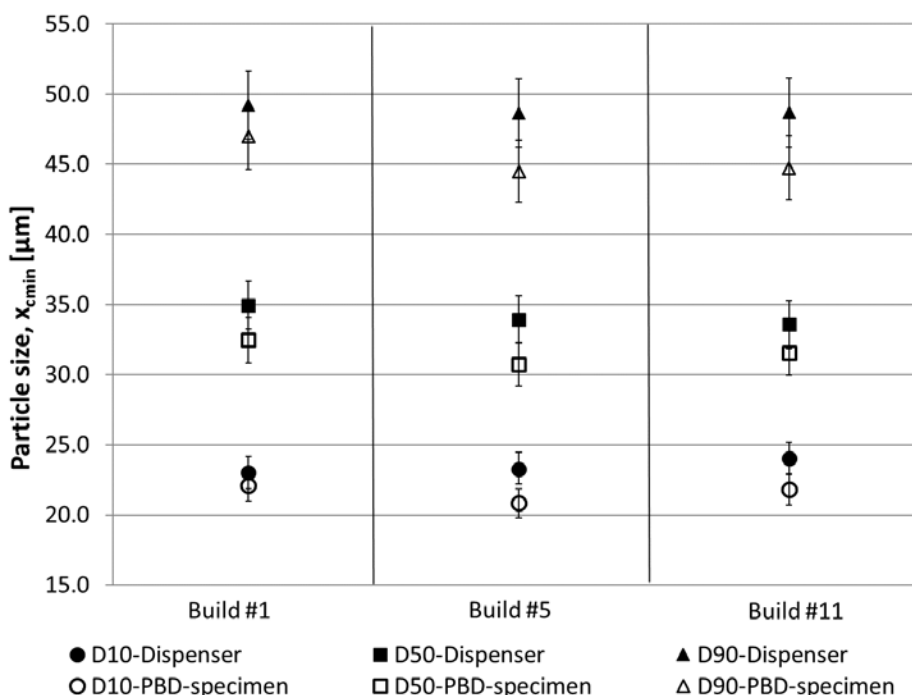
Figure 29: Comparison of particle size between powder from Dispenser Bin, and PBD specimens for Builds #1, #5, and #11, powder samples with values of D_{10}, D_{50}, and D_{90} (Average ± 5 % measurement uncertainty) of particle size.

3.1.3. Apparent Density and Flow Rate

The Hall funnel tests indicated that the powder samples taken from the early Builds #1 and #2 did not flow well, but the powder flow improved with the increasing number of builds. This trend can be seen in Figure 30 where the flow time decreased with increasing number of builds. This trend may be attributed to reduced humidity in the powder as it was kept in the build chamber for a longer period of time through consecutive builds. A change occurred after Build #5 where the flow time increased for Build #6. This is most likely due to the introduction of virgin powder during Build #5. It is important to note that since the powder sample was skimmed from the top of the dispenser bin, the results of the apparent density and flow rate measurements only reflect those layers of powder, which are recycled from the previous build. In the case of Build #6, the analyzed powder is a mixture of different powder portions, which were combined after the Build #5. In this case the powder mixture is composed of 41 % of the four-time recycled powder from Build #4, 36 % of the once-recycled powder from Build #1, and 23 % of virgin powder (see Figure 7).

24
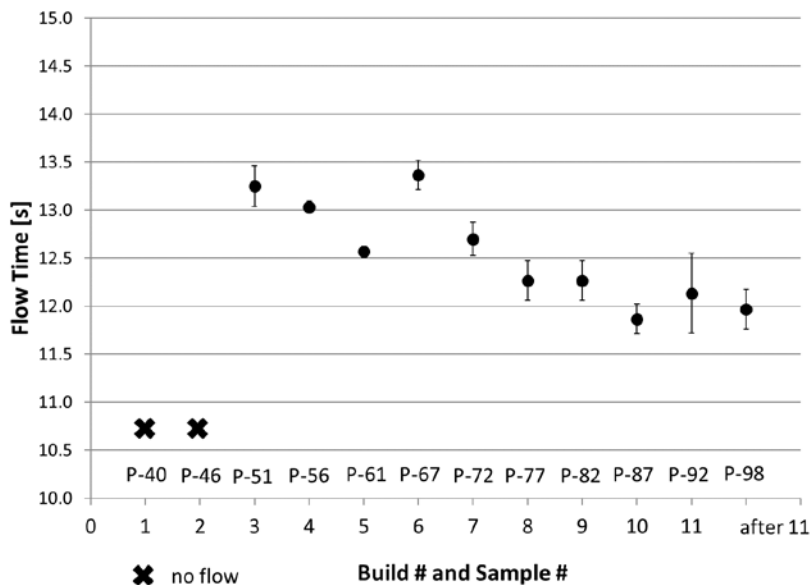
Figure 30: Flow time for powder samples corresponding to different builds (error bars are one standard deviation).

Apparent density (AD) increased for the dispenser bin powder with increasing number of builds (Figure 31). There was a decrease in apparent density measured before Build #6 has started, since virgin powder was introduced into the "recycled*" powder during build #5. It appears that "refreshing" the entire powder volume with 23 % virgin powder in Build #5 can be detected in this measurement by an increase of the measured flow time and at the same time a decrease of the apparent density of the powder for the next build (Build #6, sample P67), as shown in Figure 31.
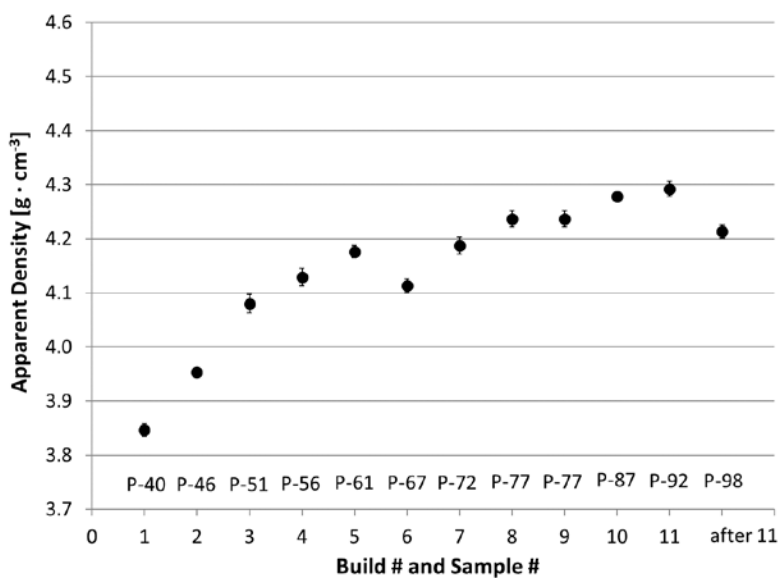
Figure 31: Apparent density of sampled powder from dispenser bin (error bars are one standard deviation).

25

3.1.4. Powder Bed Density

Particle size distribution, morphology, and humidity content are likely to influence the spreading of the powder on the build platform, resulting in potentially varying powder bed density (PBD). PBD measurements were conducted for three different build conditions. It should be noted that the combinations of the different powder portions as described earlier (Figure 7) refer to the entire powder volume on the build platform, but not for the powder that is captured inside the PBD capsules. Depending on the changing cross-section of the inner cavity of the PBD capsule along the building height, the amounts of different powder portions inside the cavity vary with respect to the overall powder portions on the build platform. PBD measurements were conducted to the three different enclosed powder compositions:

- Build #1 consists of 100% virgin powder

- Build #5 consists of approximately 51% from previous Build #4 (recycled four times), approximately 46% from Build #1 (recycled once), and approximately 3% of virgin powder

- Build #11 consists of approximately 51% from previous Build #10 (recycled ten times), approximately 46 % from Build #5 (recycled five times), and approximately 3% of virgin powder

Three PBD capsules were fabricated on each build plate, which were used for PBD measurements. The measurements indicate that powder recycling has an effect on the PBD (Figure 32). The expanded uncertainty (k=2) associated with the PBD measurements is 0.004 g · cm 3 (or about 0.1%) [Jacob et al., 2016]. Although Builds #5 and #11 have about the same relative amounts of virgin powder and five times recycled powder, the remaining powder is recycled once (for Build #5) or ten times (Build # 11). There is an approximate difference of 1.6 % in PBD between these two builds. The difference between Build #1 and Build #5 is even greater (2.3 %).

As shown in Figure 28 and Figure 29, the particle sizes and PSD of powder in PBD capsules do not significantly change between Builds #1, #5, and #11. The slight change from coarser distributed virgin powder (P-40) in Build #1 to a finer distributed recycled powder (P-92) in Build #11 is in the range of the measurement uncertainty (± 5 %). Hence, the increase in PBD, shown in Figure 32, cannot be explained by particle size characteristics. It is possible that other powder characteristics like moisture content, which were not investigated in this study, have more of an impact on these powder properties like flowrate and apparent density, which in turn affects the powder spreading on the build platform. Continued exposure in the warm build chamber environment possibly removes moisture from the powder that would lead to an improved flow, higher apparent density, and an increase in the PBD.
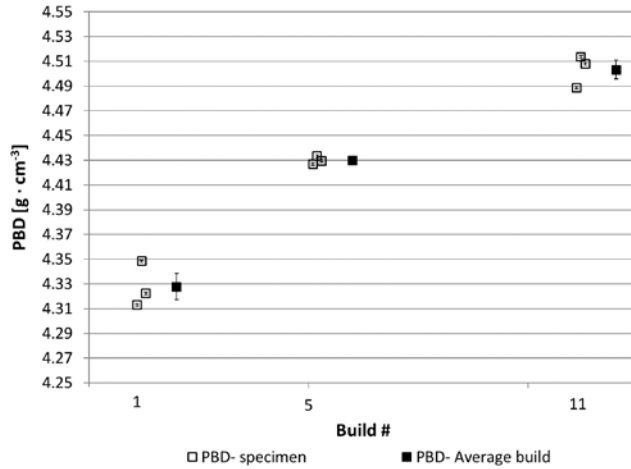
Figure 32: Comparison of PBD corresponding to varying amounts of recycled powder, error bars are combined uncertainty (U_{PBD}).

Figure 33 compares the apparent density (AD) of the powder taken from the dispenser bin and of the powder from the PBD specimens from Builds #1, #5, and #11. The increase of the AD over the number of builds is consistent with the increase of the PBD. Overall higher PBD levels compared to AD is due to the packing of powder during the recoating process. Therefore, PBD is considered to be close to the tap density (TD) of powder. The apparent density between Build #1 and Build #5 increases about 8.6 % from 3.85 g cm^{-3} to 4.18 g cm^{-3} and further 2.6 % from Build #5 to Build #11 of 4.29 g cm^{-3}. The PBD does increase in comparison only of approximately 2.3 % from 4.33 g cm^{-3} from Build #1 up to 4.43 g cm^{-3} from Build #5, and further 1.6 % up to 4.5 g cm^{-3} from Build #11. It appears that recycling caused larger changes in PBD compared to the changes in AD.
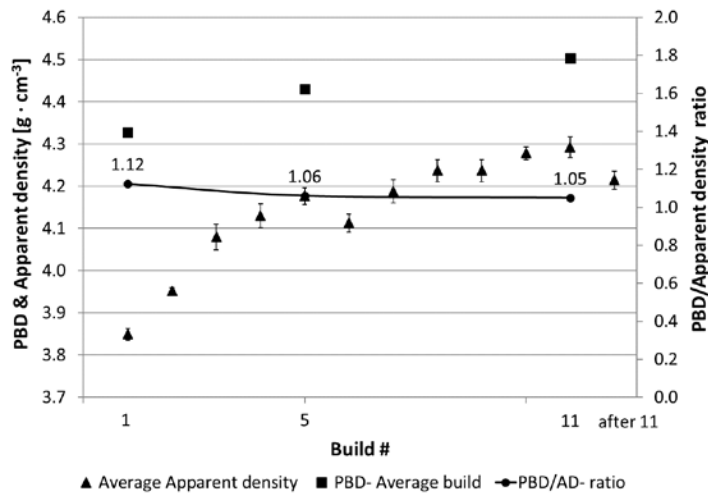
Figure 33: Comparison of PBD and AD of sampled powder (error bars are one standard deviation) with the ratio of PBD and AD.

27

The ratio between the TD and AD, called the Hausner Ratio, is used to assess the flowability of metal powder [*Abdullah et al., 1999*]. Lower values of this ratio indicate better flowability. Figure 33 shows that the PBD/AD ratio decreases with the number of recycling the powder. This supports the observations of the flowrate measurements using Hall funnel tests of the powder samples [*ASTM B213, 2013*]. The powder samples from Build #1 and Build #2 (P-40, and P-46) did not flow through the lower funnel opening, even after tapping the funnel, while powder sample from Build #5 flowed through the funnel freely. Beside the correlation between a decreasing PBD/AD ratio with the number of builds, these results also show good correlation between the determined AD measured with the established Hall Funnel Test and the achieved PBD under real process conditions inside a PBF machine.

3.1.5. Powder microstructure

The crystal structure of powder samples was examined by using X-ray diffraction (XRD) analysis. The calculated volume fraction of FCC austenite and the diffraction patterns obtained from the select samples mentioned in Table 4 are shown in Figure 34. As shown in Figure 34, considering the measurement uncertainty, the change in volume fraction of FCC austenite over the multiple builds is not significant. This figure also shows that FCC austenite is the predominant phase in the S17-4 PH powder (above 90 %), which is consistent with the results reported in literature [*Murr et al, 2012*].
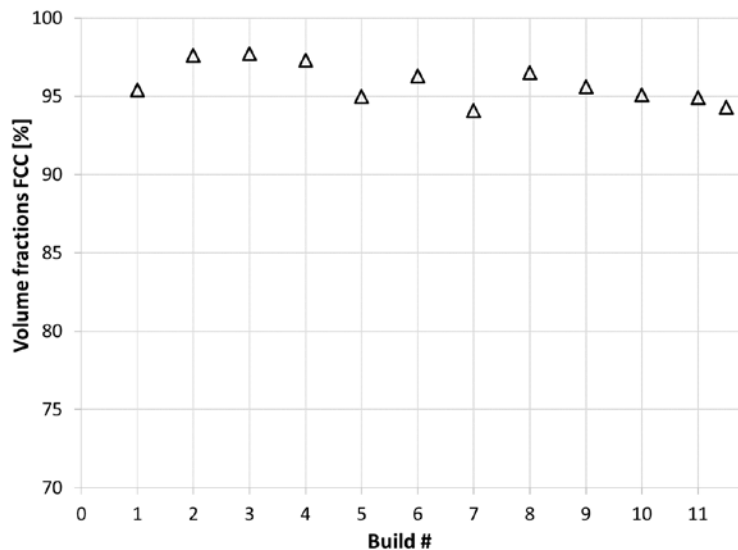
Figure 34: Calculated volume fraction of FCC austenite in used S17-4 PH powder over build number. The calculated results have an uncertainty in volume fraction of approximately ± 10%.

Figure 35 shows the XRD pattern of P-40 (virgin), and P-98 (eleven times recycled) from the dispenser bin. The XRD patterns have strong Bragg reflections ɣ (111), and ɣ (200), which correspond to the predominant FCC austenite phase. The magnified view of the same XRD pattern (see Figure 36) shows a relative increase in the BCC ferritic-martensitic phases of the multiple times recycled powder (P-98) according to the Bragg reflection α (110). Figure 37 shows that even the four times recycled powder (P-61) for the Build #5

has a slight increase in BCC phase compared to the unused virgin powder (P-40), while further use/recycling of the S17-4 PH powder (P-92) did not further increase the amount of BCC phases. Similar results were also presented by *Slotwinski et al.* [*2014*]. **Figure 38** shows the comparison of XRD patterns of powder samples from the dispenser bin (before and after the build) and the PBD capsule of Build #11. These results show no obvious differences in the XRD patterns.
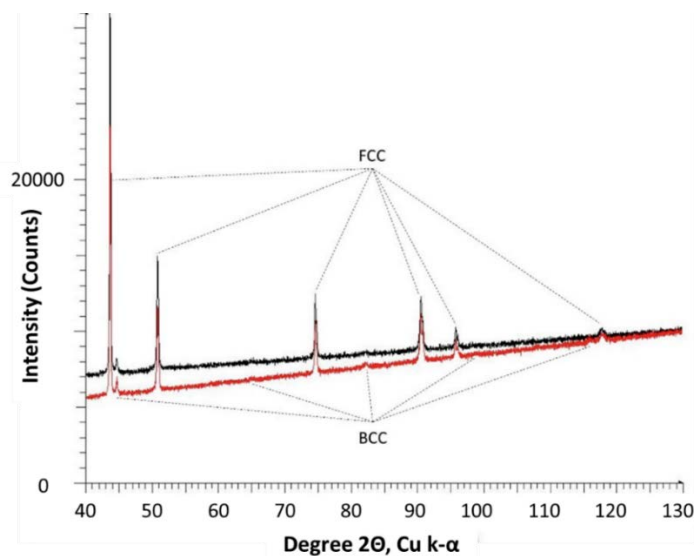
Figure 35: Comparison of X-ray diffraction patterns of sample P-40 (red, virgin powder from Build #1), and P-98 (black, after Build #11).
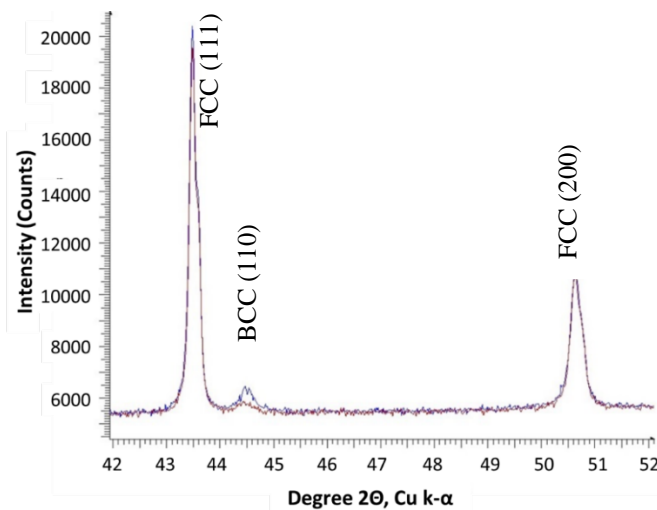
Figure 36: Expanded and scaled view of the differences between P-40 (red, virgin powder from Build #1) and P-98 (blue, after Build #11).
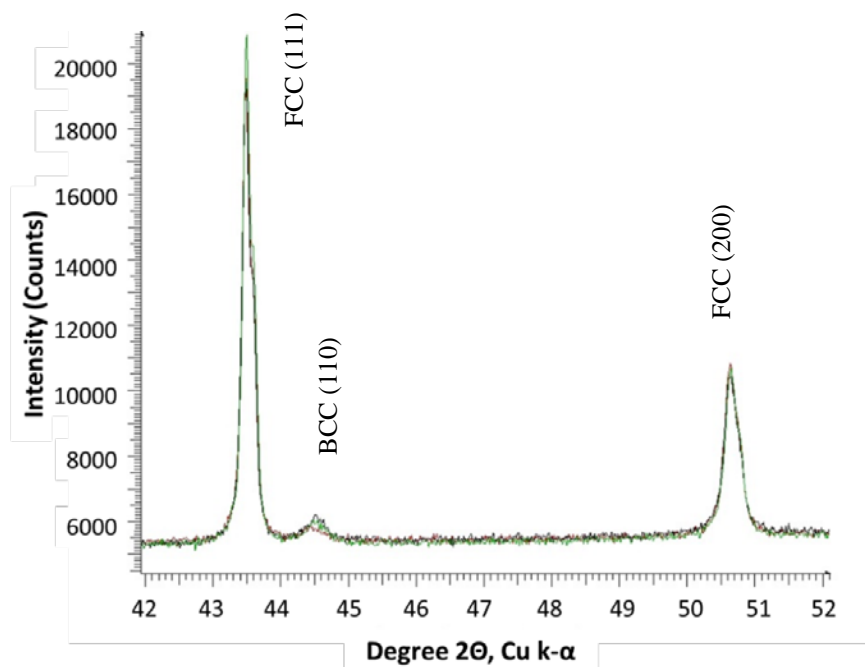
Figure 37: Comparison of X-ray diffraction patterns from dispenser bin powder samples P-40, VIRGIN, (red trace, Build #1), P-61, RECYCLED (green trace, Build #5), and P-92, RECYCLED, (blue trace, Build #11).
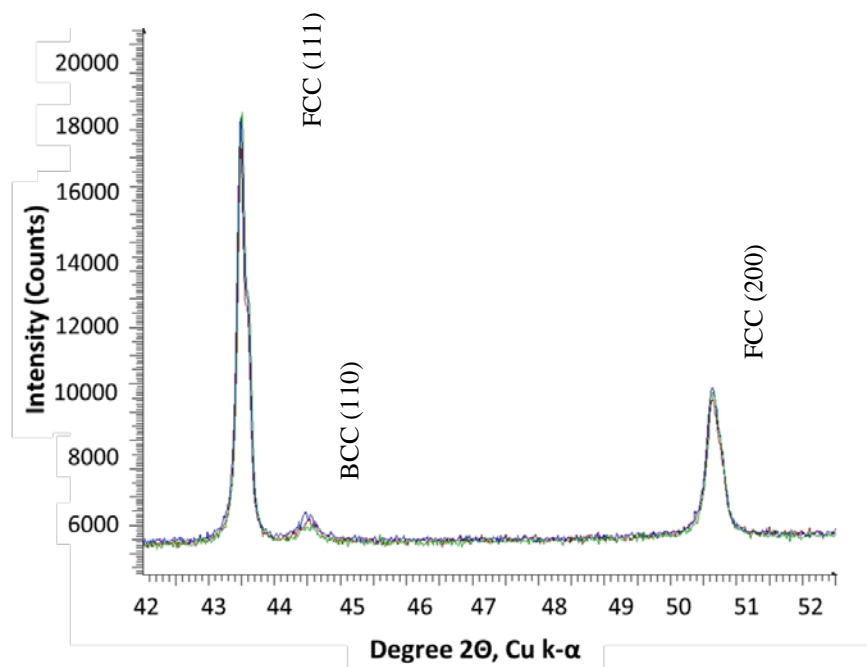
Figure 38: Build #11, powders from the dispenser bin (P-92, red), the PBD (P-96, blue), and after build, dispenser bin, sieved (P-98, green) show a decrease in BCC peak intensity for the sieved dispenser powder.

3.1.6. Powder chemical composition

Chemical analysis of powder samples was conducted by a commercial service laboratory following standard procedures identified in ASTM E1019 [*2011*] and ASTM E1086 [*2014*]. Table 5 shows the results of this chemical analysis.

Table 5: Chemical composition of virgin and recycled S17-4 PH powder (mass %).

Element content	UNS S17400 Type 630 Specified limits (ASTM A564/ A564M-13)	Virgin Powder; P-40 build #1	Recycled Powder; P-92 build #11
Carbon; C	0.07	0.03	0.03
Manganese: Mn	1.00	0.67	0.72
Phosphorus; P	0.04	0.016	0.017
Sulfur, S	0.03	0.006	0.006
Silicon, Si	1.00	0.8	0.73
Nickel, Ni	3.00 to 5.00	4.81	3.9
Chromium, Cr	15.00 to 17.50	15.72	15.12
Molybdenum, Mo	…	0.11	0.12
Copper, Cu	3.00 to 5.00	3.74	3.41
Nitrogen, N	…	0.16	0.16
Tantalum Ta + Niobium Nb	0.15 to 0.45	…	…

Both powder samples are within the specified limits, and no difference was observed in the chemical composition between the virgin powder from Build #1 and the recycled powder from Build #11. Based on these results, recycling powder in a laser-based PBF process including the accumulated laser exposure time in a nitrogen atmosphere, does not dramatically affect the chemical composition for the S17-4 PH powder material. Since the LPBF process takes place in an environment with small amounts of oxygen, in future studies, oxygen content of the samples may also be investigated to verify this conclusion.

3.2. Analysis of manufactured specimen properties

3.2.1. Surface roughness

A white light interferometer was used to measure the roughness of the "as-manufactured" two witness cube faces: the top surface (xy-plane) and the vertical surface (xz-plane). Three roughness scans were conducted on each surface as shown in Figure 39. For the top surface, three locations were scanned using a 10x magnification objective, each covering an approximate area of 2 mm x 2 mm. An example of one of these areas is shown in Figure 40. Three profiles were obtained from each location surface topography data (Figure 40C). The measured surface topography either of the xy-plane and xz-plane is shown in Figure 40 and in Figure 41. Averages were computed out of these nine combined scans and the

associated profile roughness parameters Ra and Rz of the Builds #1, #5, #6, and #11 are presented in Figure 42 and Figure 43.
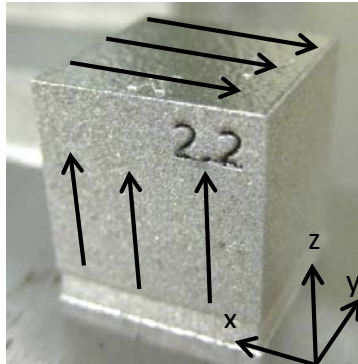
Figure 39: Schematic of surface roughness measurement locations on witness cube planes.

For the vertical surface (xz-plane), since the surface is rougher and to improve the interferometry, a 50x magnification objective was used covering an approximate area of 0.375 mm x 0.375 mm. In order to obtain roughness information over a larger area, 28 of these areas were stitched to create a topographical data field over an area of 0.375 mm x 4.5 mm, which is shown in Figure 41A. Three such stitched area topographies were created over the vertical surface. Three separate surface profiles along the z-axis (build direction) were obtained from each stitched topography (see Figure 41C).

Figure 42 and Figure 43 indicate that the top surfaces of the cubes are smoother than the vertical surfaces. This is expected since according to the process recipe provided by the machine vendor, for the layers within the top 0.1 mm, scan parameters were chosen to obtain a smooth top surface (called "upskin" parameters). Specifically, the laser power was decreased from 195 W down to 160 W and the laser scan speed was reduced by half, from 1000 mm s^{-1} to 500 mm s^{-1}.

The roughness of both horizontal top surface and the vertical surface did not change as the powder was recycled multiple times. The roughness results from each build are within the variance of the other builds.
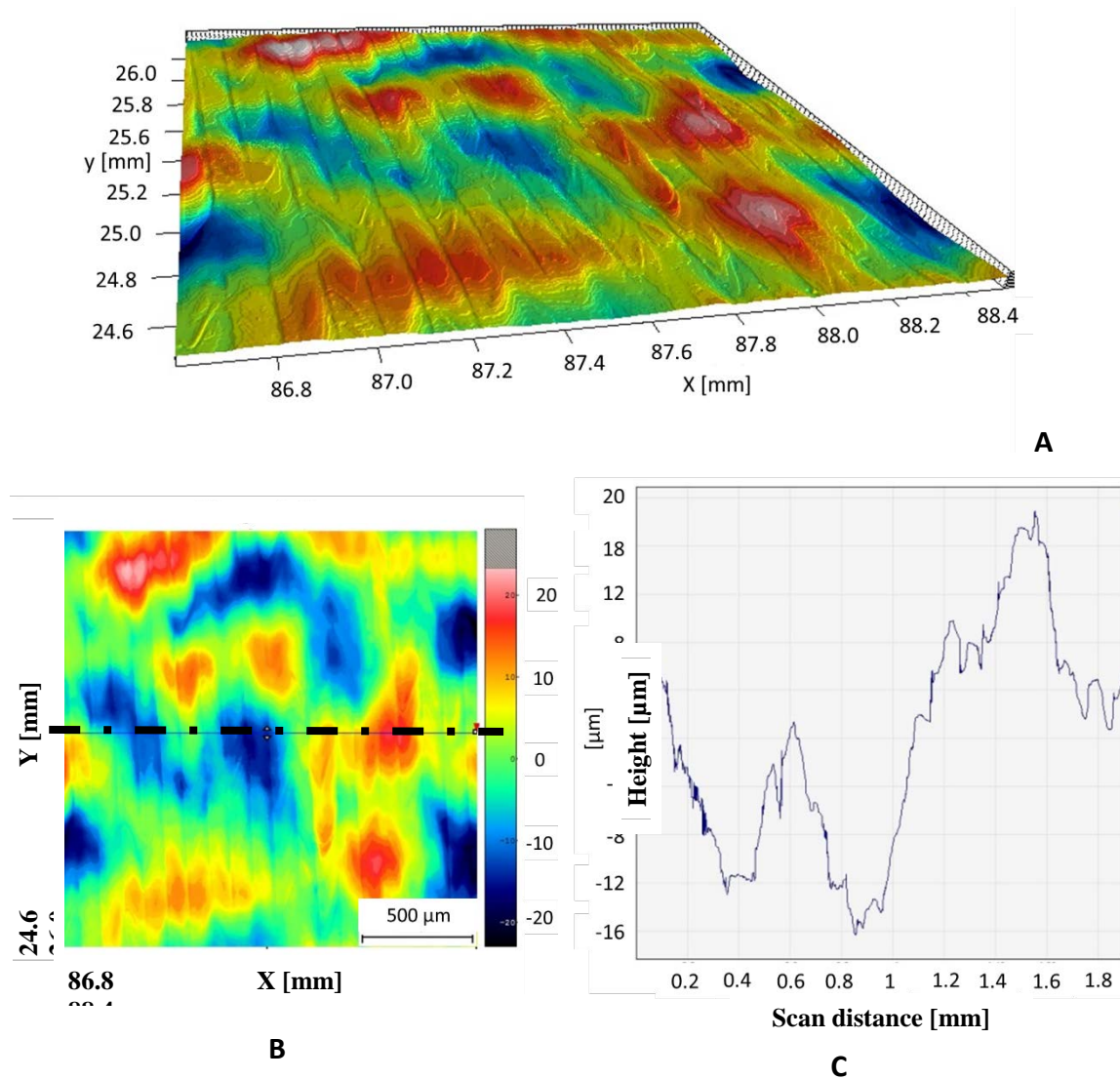
Figure 40: A) 3D surface topography of xy- plane from a witness cube, B) 2D topography of the same surface in A, C) H- profile line of the marked scan line in B.
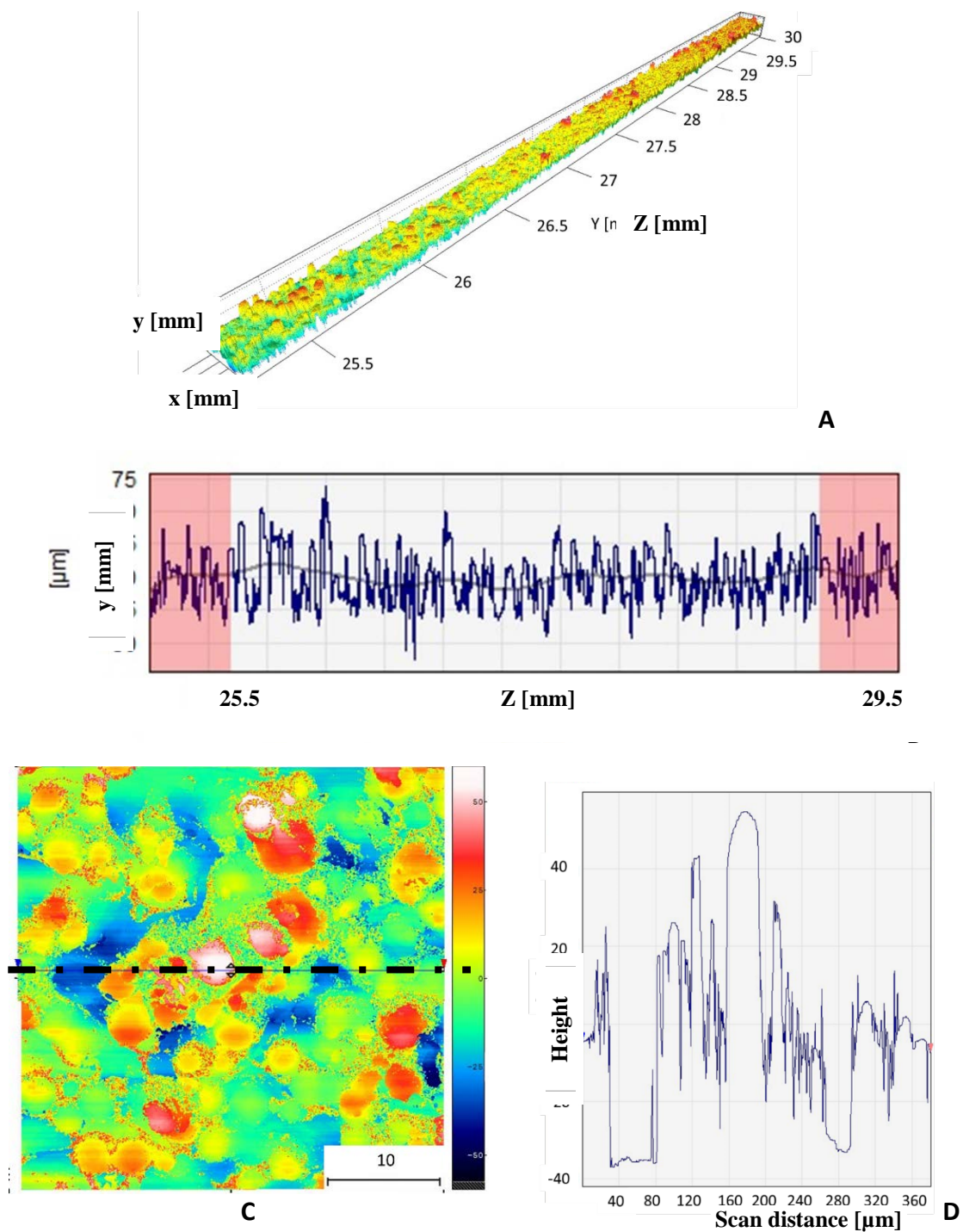
Figure 41: A) 3D surface topography of xz- plane from witness cube (Build #5) along 4.8 mm scan length. B) H- profile line of surface topography over a 4.8 mm scan length 2D representation of a magnified area (378 μm x 378 μm) in the xz-plane.
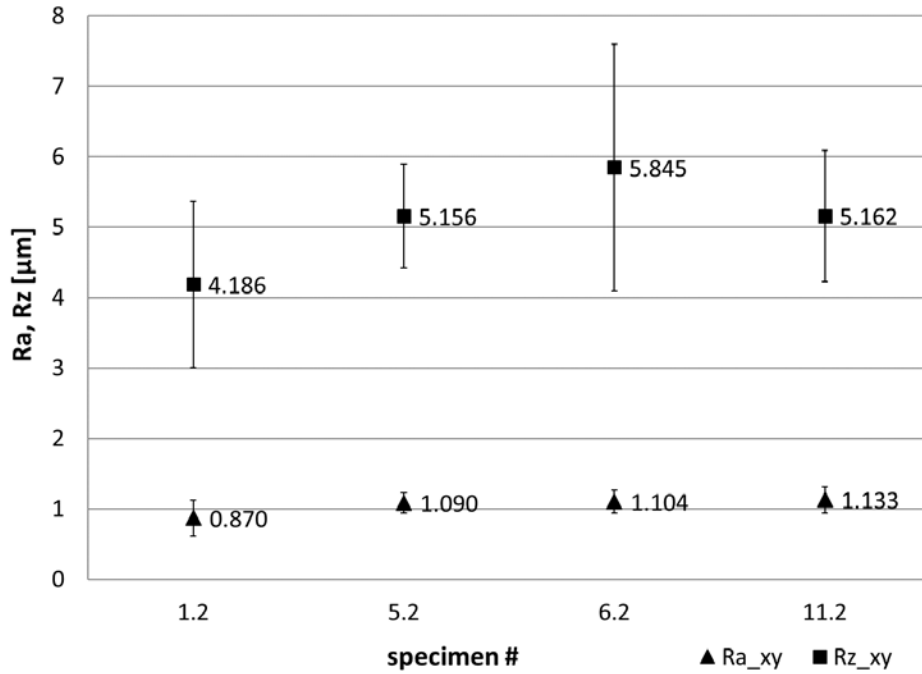
Figure 42: Surface roughness on xy- plane, error bars show ± one standard deviation.
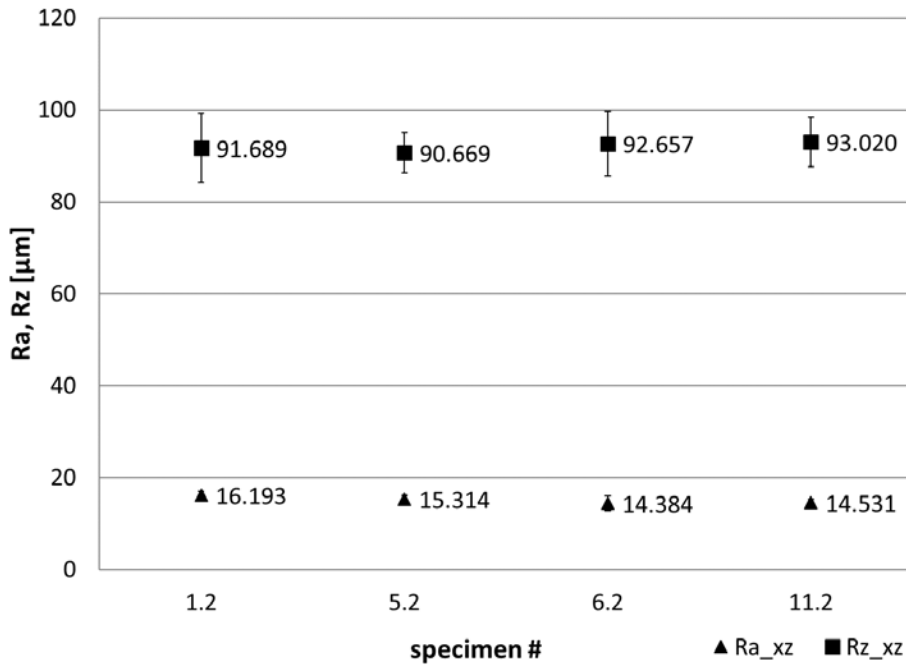
Figure 43: Surface roughness on xz- plane, error bars are ± one standard deviation.

35

3.2.2. Bulk Density

The density of the solid S17-4 PH material (bulk density) was determined based on the Archimedean Method, according to ISO 3369 [*2006*]. All three witness cubes from each build were measured to obtain the average density for each build (Figure 44).

Build	Average [g cm^{-3}]	relative [%]
1	7.897	99.97
2	7.902	100.03
3	7.873	99.65
4	7.874	99.67
5	7.896	99.95
6	7.884	99.80
7	7.873	99.66
8	7.874	99.67
9	7.863	99.53
10	7.868	99.60
11	7.888	99.85
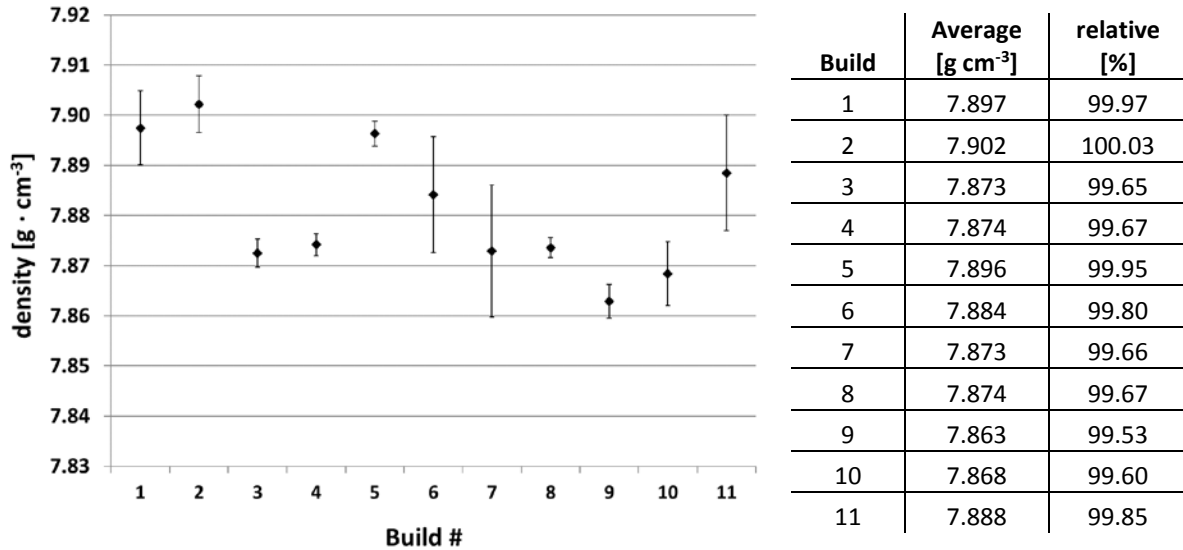
Figure 44: Averaged bulk density of witness cubes, error bars are ± one standard deviation.

The relative density for the entire build series was between 99.5 % and 100 % of the specified density of 7.9 g cm^{-3} for S17-4 PH according to the vendor material specification [*EOS, 2014*]. A decrease in density was observed for Builds #3 and #4. In contrast to the witness cubes from Builds #1 and #2, the cubes from Builds #3 and #4 were mostly made out of recycled powder from the previous build and only approximately the last 2 mm on top were fabricated out of the recycled powder from the Build #1. This was also similar for the cubes in Build #5. The bulk density of Build #5 cubes is similar to the first two builds. Therefore, a clear correlation between the changed bulk density over the first five builds is not identified. The trend of a decreasing density over Builds #6 to #10 may be explained by an increase of particle sizes of these powders used to manufacture the witness cubes [*Kruth et al., 2007*]. The rise of the bulk density in Build #11 despite the decreasing density of the previous builds is unclear, because the witness cubes in Build #11 were also made out of recycled powder from the previous Build #10. Considering the variance of the bulk density, there does not appear to be a correlation between the powder characteristics from recycling the powder on the measured bulk density. The density variation between the builds may be randomly distributed and caused by the measurement procedure of the Archimedean Method. Variation may be related to the water temperature measurement, measuring the specimen mass in and out of the deionized water, and specimen buoyancy caused by the surface tension between the specimen surface and trapped air bubbles. Like the surface roughness of the "as-manufactured" S17-4 PH solid material, the bulk density measurement on the manufactured S17-4 PH shows no significant change with increasing amount of recycled powder during the series of builds.

3.2.3. Tensile strength

All tensile specimens of each build were stress relieved according to the heat treatment regime as described previously. At least three tensile specimens, but no more than five, from each build were tested in tension until failure (Table 6, Figure 45 to Figure 47). The stress-strain curves based on the extensometer signal exhibit typical behavior for chromium-nickel stainless steel (see Figure 48 to Figure 53).

Table 6: Results of the tensile tests, average, AVG, and expanded uncertainty of average, U (k=2).

Build	UYS [MPa] AVG	U	$YS_{0.2}$ [MPa] AVG	U	UTS [MPa] AVG	U	A [%] AVG	U	E [GPa] AVG	U
1	622	7	591	38	1327	2	28	0.4	184.2	5
2	604	15	589	14	1325	27	24	5	185.7	5
3	608	12	596	35	1335	13	26	1	185.9	3
4	594	23	573	24	1350	40	24	3	188.7	15
5	606	23	580	58	1340	34	26	4	188.7	14
6	624	12	595	17	1329	24	28	1	192.3	17
7	589	21	570	13	1380	15	26	4	187.6	16
8	588	12	558	18	1368	24	24	1	190.1	7
9	593	12	574	10	1355	23	23	3	181.4	12
10	594	37	573	52	1343	57	25	1	189.4	12
11	618	5	593	24	1331	18	27	1	188.3	20
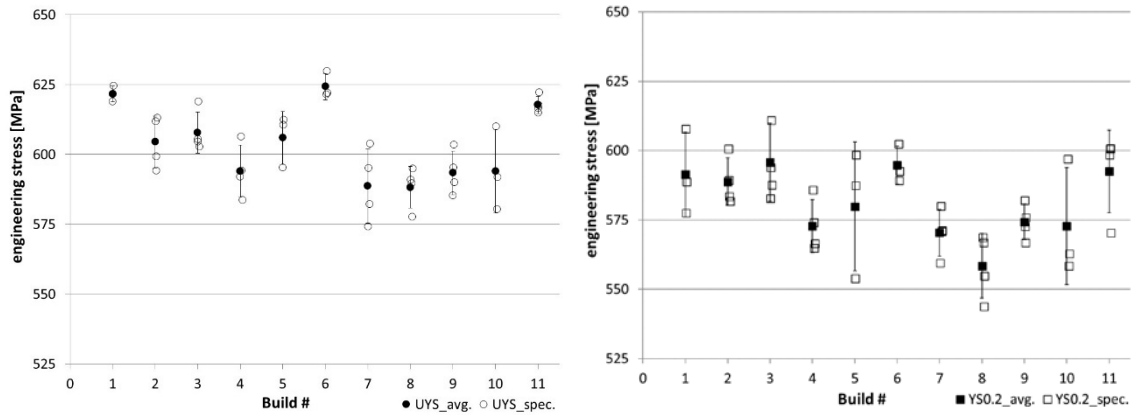
Figure 45: Upper yield strength (UYS) left and 0.2 % Offset Yield Strength ($YS_{0.2}$) right, error bars are one standard deviation (SDEV.S).
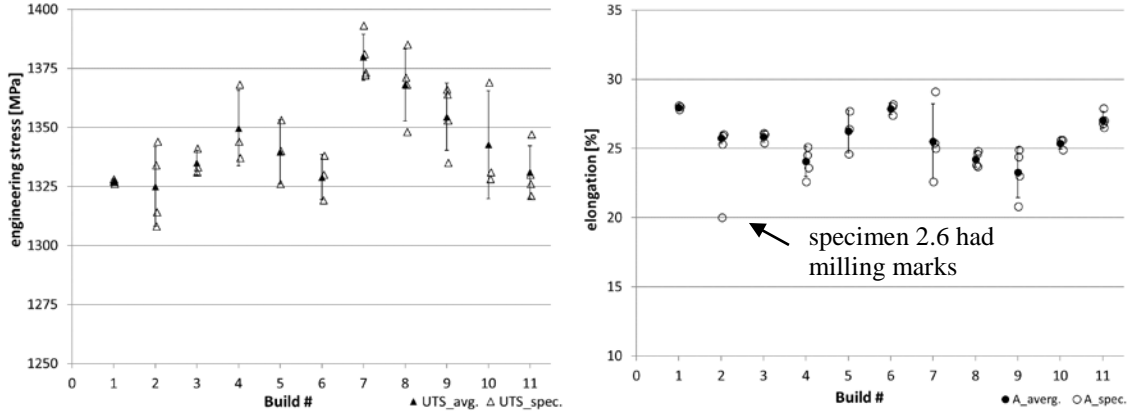
Figure 46: Ultimate tensile strength (UTS) left and Elongation after failure (A) right, error bars bars are one standard deviation (SDEV.S).
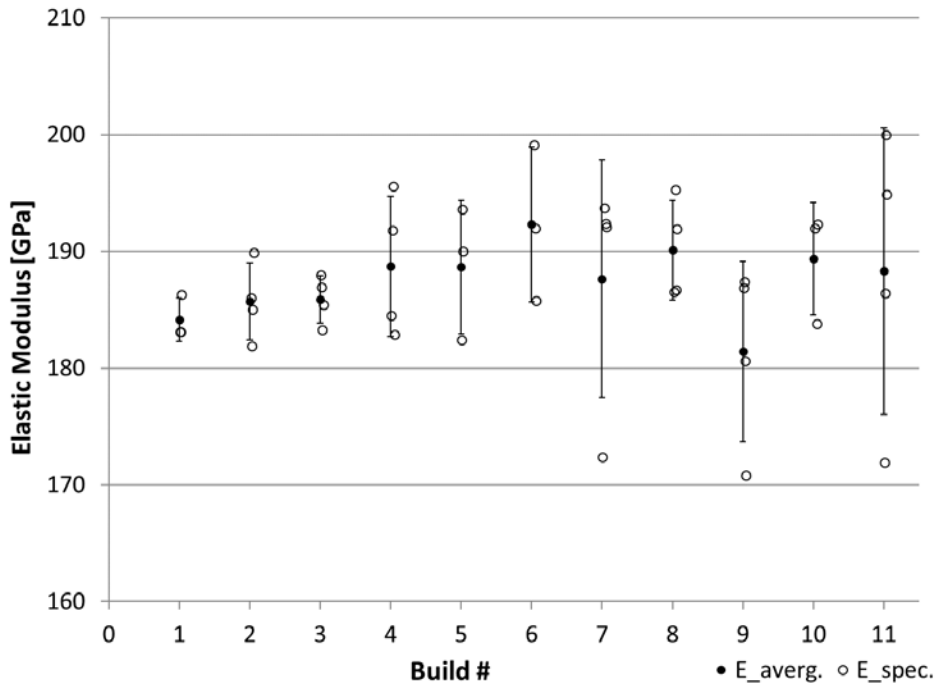
Figure 47: Elastic Modulus (E), error bars bars are one standard deviation (SDEV.S).

The tensile properties may be affected by the powder as it was recycled, however the relationship is not clear. Figure 45 shows the results of UYS and $YS_{0.2}$ for all eleven builds. The UYS in build #1, #6, and #11 is higher than the others. However, there is no clear correlation between the powder conditions corresponding to these builds and the other builds. All tested specimens reached a value of $YS_{0.2}$ above 540 MPa.

The results of the UTS (Figure 46) show an opposite trend compared to the results of UYS and $YS_{0.2}$. UTS of Builds #1, #2, #6, and #11 is lower than the UTS from the builds between them. The lower UTS in Build #1, #2, and #6 may be explained by the different powder conditions before the powder was used to manufacture the tensile bars.

38

The elongation also shows a similar correlation to the recycled powder as the results of the UYS and $YS_{0.2}$ (Figure 45). Elongation of all stress-relieved specimens exceeded 20 %.

The elastic modulus (E) of all tested specimens was in a range from 170 GPa to 200 GPa, typical for chromium-nickel stainless steel alloys. Determining E using the tensile test may not be precise enough due to the unstable strain conditions of the material. The elastic modulus did not change over the series of builds depending on the recycled powder. The only observation from the data appears to be that the variance increases over the series of builds.

Based on the tensile test results, the effect of recycling S17-4 PH powder for the eleven builds did not significantly affect the mechanical tensile properties.

The engineering stress-strain curves of the tested tensile specimens from all builds were similar, and those plots from Build #1, Build #2, Build #5, Build #6, Build #7, and Build #11 are shown (Figure 48 to Figure 53). No significant difference between the curves was observed. All specimens exhibited discontinuous yielding after passing the upper yield strength (UYS), i.e., a constant strength during continuous yielding of the material caused by initial movement of a dislocation front (*Lüders Bands*) through the material. This is typical for soft, unalloyed steels with a low carbon content and stable austenitic-phase-dominated steels. Martensitic steels are usually characterized with high UTS and without an upper and lower yield strength (UYS and LYS) and without discontinuous yielding during the tensile test. Therefore, the plots in Figures 48 to 52 indicate a mixed phased steel. High UTS can be explained by the stress induced phase transformation of the retained metastable FCC austenite into the BCT martensite. Starr et al. [*2013*] observed such transformation in additively manufactured S 17-4 PH.
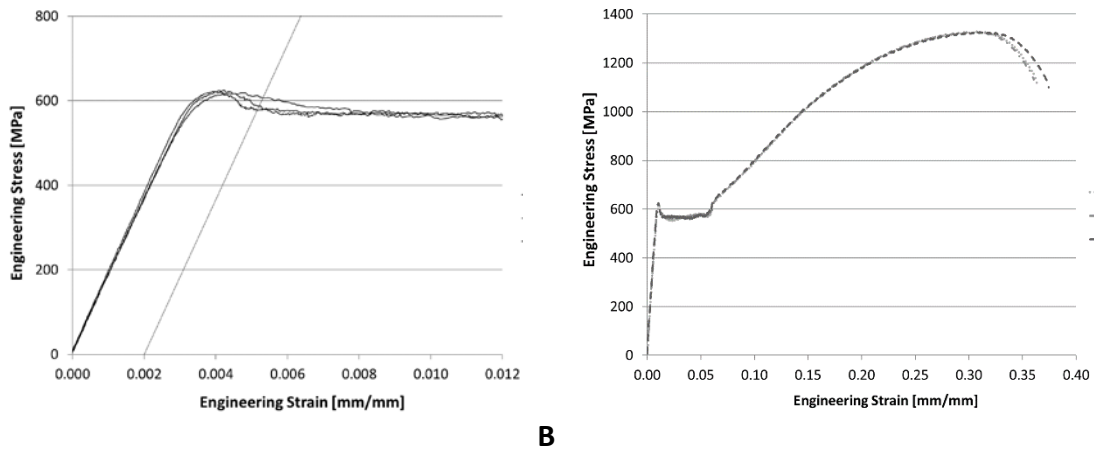
A　　　　　　　　　　　　　　　　　**B**

Figure 48: Tensile stress-strain curves of Build #1. A) The extensometer was removed after the UYS, B) UTS corresponds to maximum strain.

39
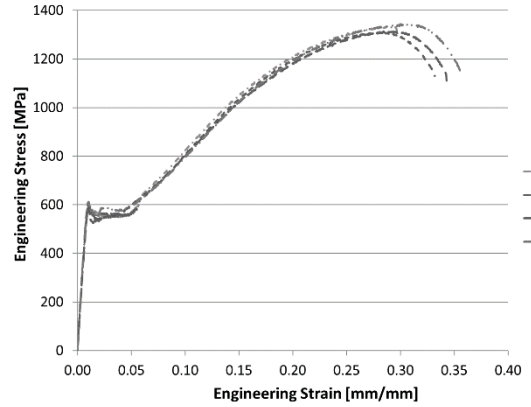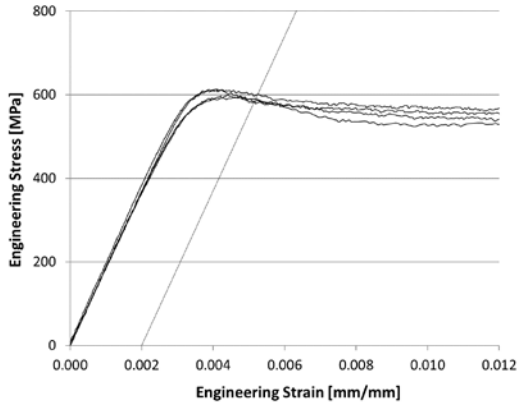
A   B

Figure 49: Tensile stress-strain curves of Build #2. A) The extensometer was removed after the UYS, B) UTS corresponds to maximum strain.
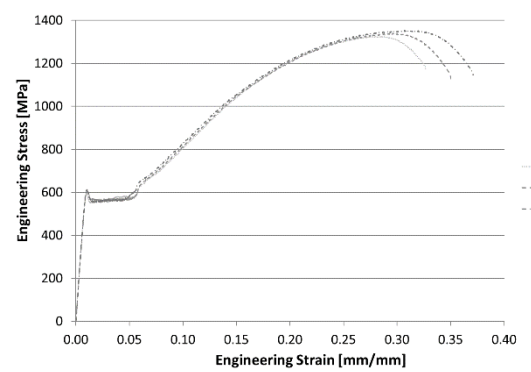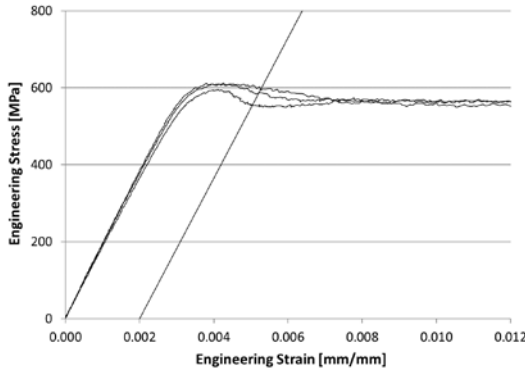
A   B

Figure 50: Tensile stress-strain curves of Build #5. A) The extensometer was removed after the UYS, B) UTS corresponds to maximum strain.
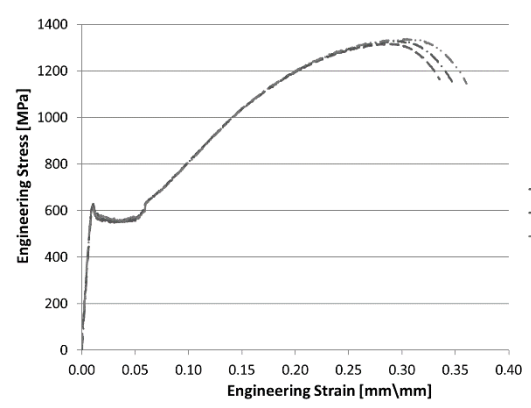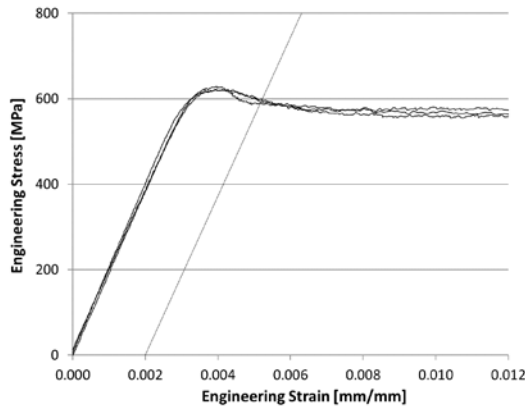
A   B

Figure 51: Tensile stress-strain curves of Build #6. A) The extensometer was removed after the UYS, B) UTS corresponds to maximum strain.
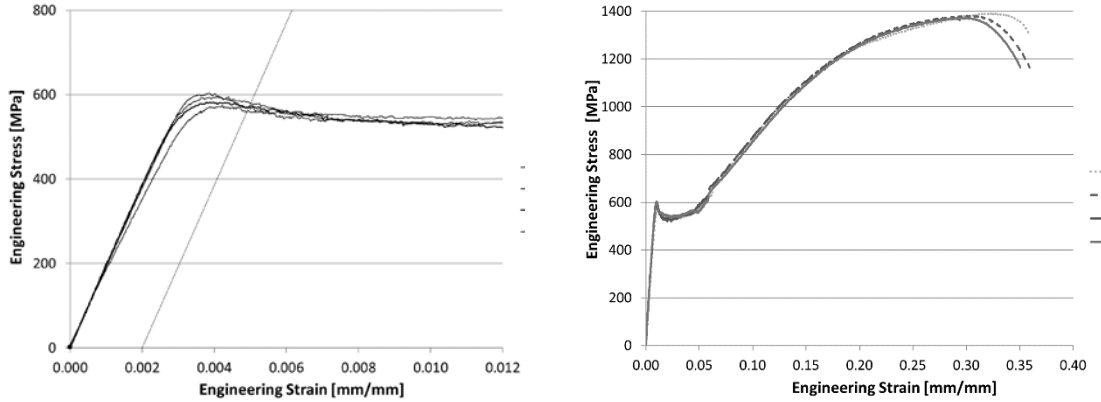
A   **B**

Figure 52: Tensile stress-strain curves of Build #7. A) The extensometer was removed after the UYS, B) UTS corresponds to maximum strain.
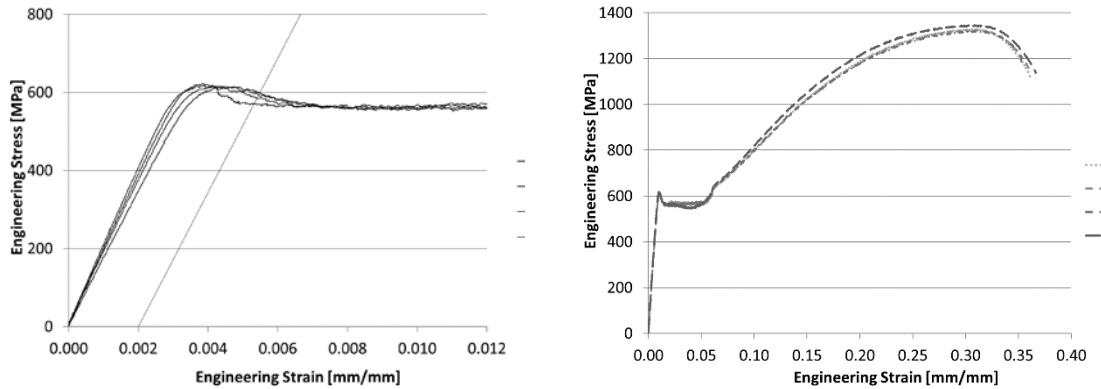
A   **B**

Figure 53: Tensile stress-strain curves of Build #11. A) The extensometer was removed after the UYS, B) UTS corresponds to maximum strain.

3.2.4.   Dynamic elastic modulus measurements (DEMM)

The results of Young's Modulus in both directions for Build #1, Build #5, Build #6, and Build #11 are shown in Figure 54. Young's modulus along the specimen width is slightly higher with a smaller standard deviation compared to the Y along the specimen thickness. The Young's modulus results of the DEMM are similar to the elastic modulus results from the tensile test (see Table 6). In both methods the specimens from build #6 have the highest average value of E or Y compared to the other builds. Young's modulus, similar to the results of E, do not show a clear correlation to the build number with the associated amount of recycled powder.

A   **B**
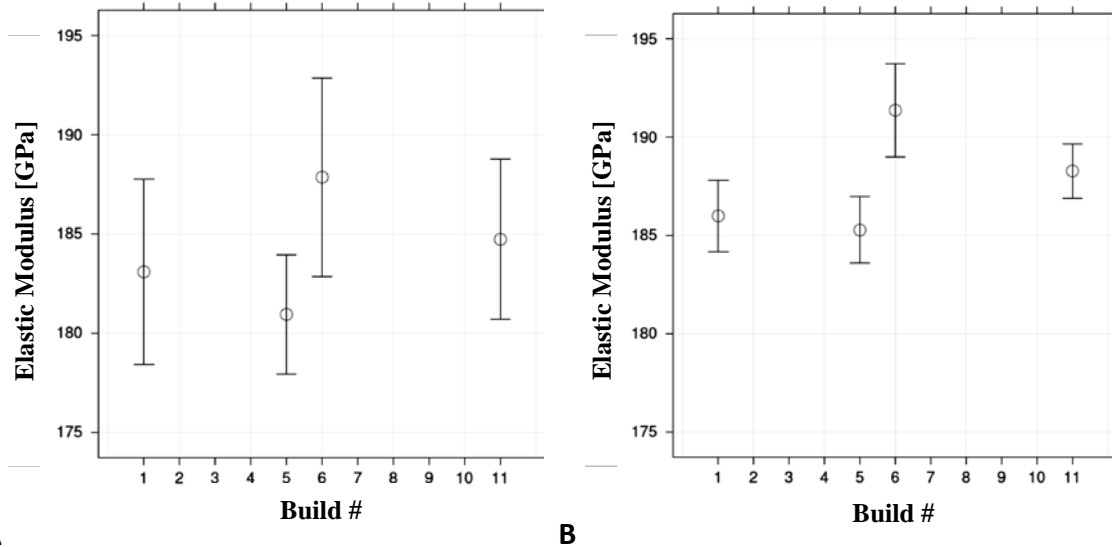
Figure 54: Results of Young's Modulus (Y) by DEMM on specimen thickness (A) and on the specimen width (B).

3.2.5. Hardness

Hardness of the witness cubes made out of virgin and recycled powder was measured using a Rockwell Hardness Tester according to the ASTM E18-16 [*2016*]. Rockwell C scale (HRC) hardness measurements were averaged based on four indents made on the vertical surface (xz- plane) of each cube.

Witness cubes were divided into two groups to investigate the effects of heat treatment for stress relief. The cubes from Builds #1, #2, #,3 and #5 were heat treated at 650 °C and slowly cooled inside the oven to relieve residual stresses. The rest of the cubes were tested in an "as-manufactured" condition. The results of the HRC measurements are shown in Figure 55.

No significant difference in HRC values within each group of cubes was observed, indicating no significant effect of powder recycling on the material hardness. HRC values corresponding to the stress-relieved group of cubes are higher than that of the as-manufactured group of cubes. A similar behavior was observed by Kumpaty et al [*2013*] where the specimens, heat treated for stress relief, showed an approximately 12 % increase of the Vickers hardness from 256.67 HV10 up to 296.33 HV10. Possible reasons for change in hardness are due to the changes in microstructure resulting from the specific procedure for stress relief heat treatment. Due to the long duration the samples are kept at high temperatures (during slow heating and cooling cycles), formation of carbides and other intermediate phases as well as martensitic transformation take place [*Seidel, 2001*]. However, as described in the Microstructure section (Section 3.2.7), measurement results indicate no significant martensitic transformation (see Figure 57). The low hardness values of as-manufactured cubes indicate that the primary austenite (FCC) phase dominates after the laser-based PBF process.

42
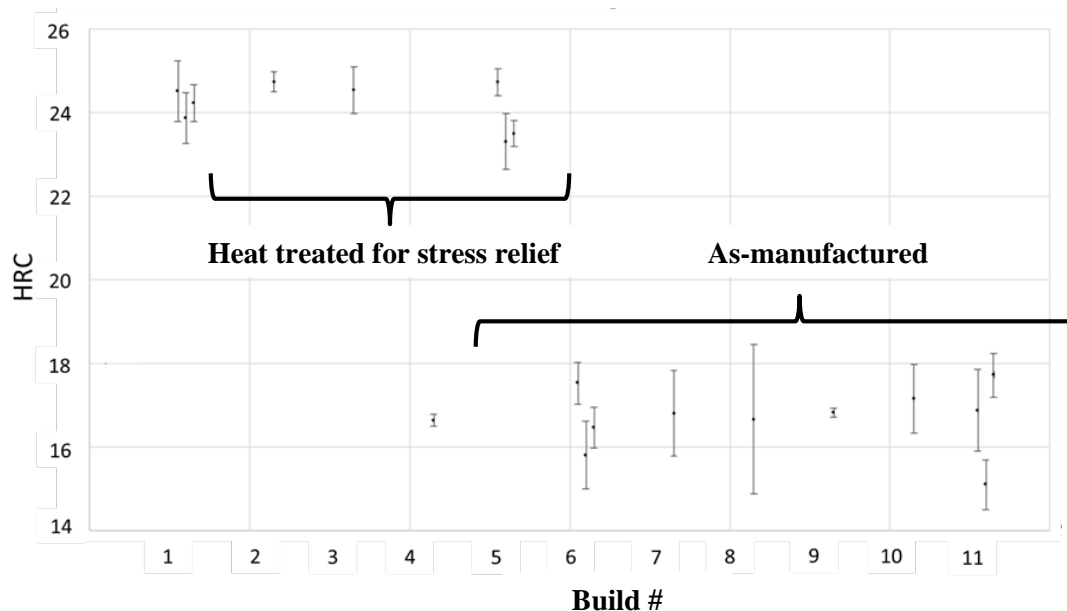
Figure 55: Hardness (HRC) results on "as-manufactured" and stress-relieved S17 4 PH specimens.

3.2.6. Chemical content

The chemical analysis results and the chemical composition limits for the UNS S17400, are shown in Table 7.

Table 7: Chemical composition of UNS S17400 and S17-4 PH solid material (mass %)

Element content in percent [%]	UNS S17400 Type 630 Specified limits (ASTM A564 / A564M-13)	Solid S17-4 PH Build #1	Solid S17-4 PH Build #11
Carbon; C	0.07	0.06	0.06
Manganese; Mn	1.00	0.52	0.3
Phosphorus; P	0.04	0.011	0.017
Sulfur; S	0.03	0.006	0.006
Silicon; Si	1.00	0.54	0.52
Nickel; Ni	3.00 to 5.00	3.58	4.7
Chromium; Cr	15.00 to17.50	16.52	16.54
Molybdenum; Mo	…	0.1	0.11
Copper; Cu	3.00 to 5.00	4.71	4.17
Nitrogen, N	…	0.15	0.15
Tantalum Ta + Niobium Nb	0.15 to 0.45	…	…

Both solid samples were found to be within the specified limits, and no significant difference was observed in the chemical composition between the "as-manufactured" S17-4 PH made out of virgin powder from Build #1 and the "as-manufactured" S17-4 PH made of recycled powder from Build #11 (mixture of 5-time and 10-time recycled powder, see Figure 7). Furthermore, the measured chemical composition of both powder and solid material correlate with each other. Based on the results, it appears that recycling powder

43

in a laser-based PBF process, including the accumulated laser exposure time in a nitrogen atmosphere, does not dramatically affect the chemical composition of the resulting S17-4 PH solid material.

3.2.7. Microstructure

Figure 56 presents the microstructure of "as-manufactured" S17-4 PH steel using virgin powder. The build direction is up in the micrograph.

A   **B**
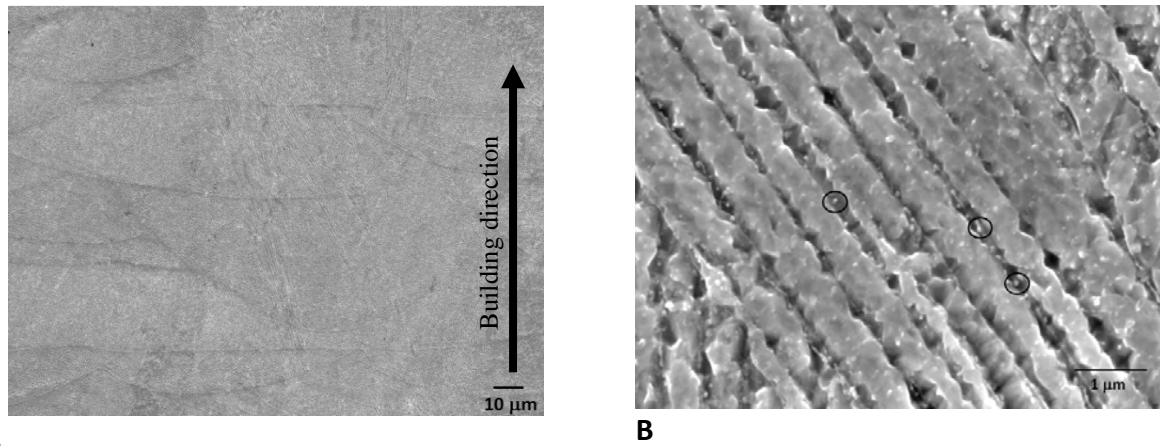
Figure 56: Microstructure of as-manufactured AM S17-4 PH steel using the virgin powder along the build direction at low magnification (A), and high magnification (B).

At higher magnification Figure 56 (B), fine dendrites/cellular solidification microstructure was observed, with a primary and secondary dendrite arm spacing of about 300 nm and 100 nm, respectively. Secondary dendrite arms are quite short, and are not clearly identifiable everywhere in the microstructure, giving rise to more of a cellular-type structure. This is due to the rapid solidification of the melt pool with cooling rate close to 10^5 K/s [*Vilaro et al, 2011*].X-ray diffraction (XRD) analysis was conducted on each witness cube to compare the changes in XRD patterns corresponding to the use of various stages of recycled powder. The XRD patterns from specimens of each build are presented in Figure 57. Note the shift in the incident angle (2Θ) position of the peaks is a result in the variation in sample height during the XRD scan and not due to a real change in lattice parameter of the phases. Although texturing and other effects can impact relative peak intensities, the ratio of FCC to BCC peak intensity indicates the amount of each phase present in the specimen material. All scans in Figure 57 (A) were performed with identical x-ray beam orientation with respect to the specimen build direction to minimize the effects of texturing on the relative peak intensities. From these relative intensities, an estimate of the volume fraction of FCC austenite and BCC ferrite-martensite was obtained over the build number, and it is shown in Figure 57 [*Cheruvathur et. al, 2015*].
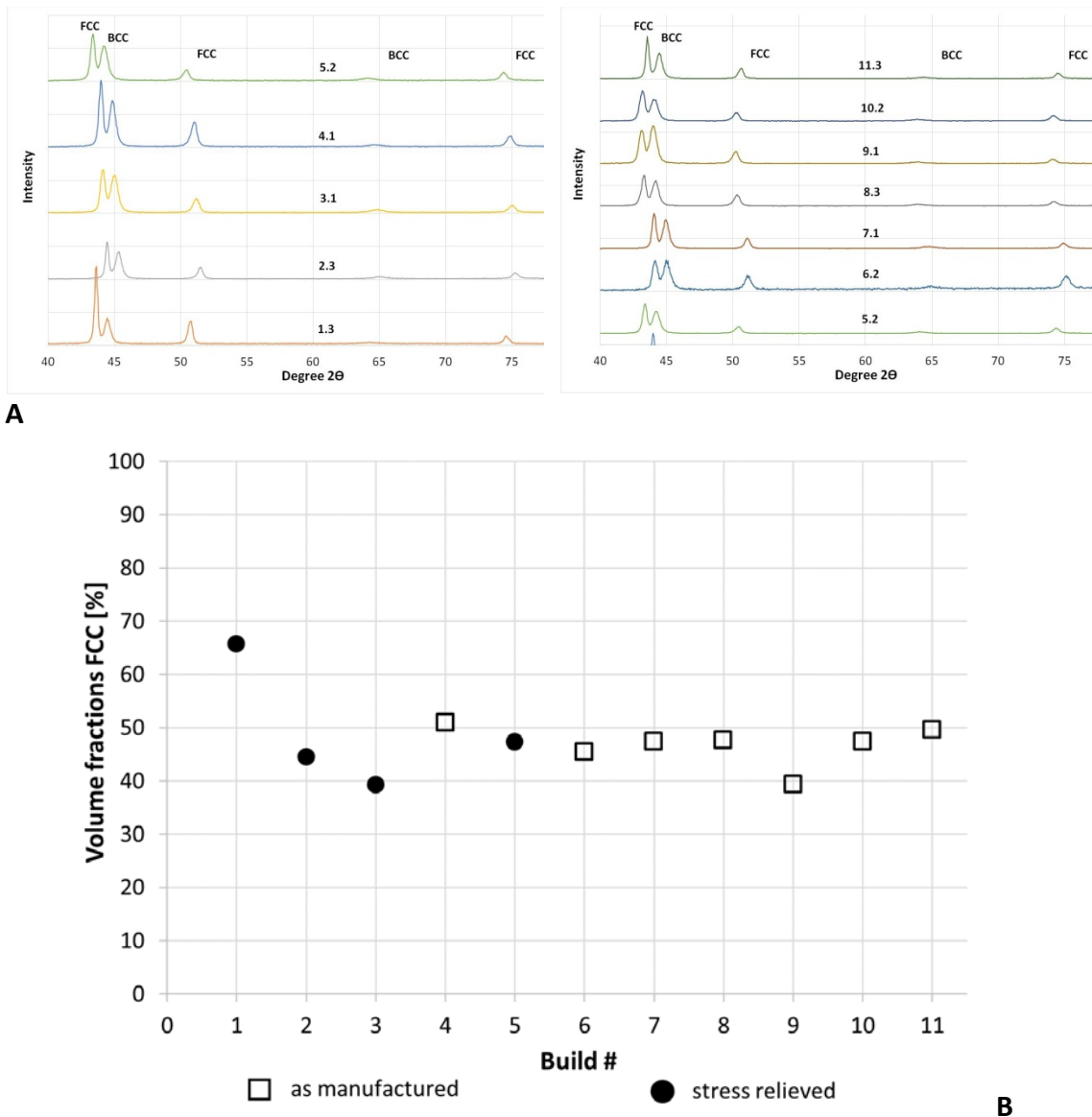
Figure 57: A) XRD patterns for samples from each of the eleven builds (1.3 through 11.3) with varying degrees of recycled powder showing the relative intensities of the FCC austenite and BCC ferrite-martensite peaks. B) The calculated volume fraction of FCC austenite in each build. The calculated results have an uncertainty in volume fraction of approximately ±10 %.

In Figure 57, specimen 1.1, made with virgin powder, from Build #1 had a microstructure with a volume fraction of FCC-austenite of about 65 %. For the remaining builds, there is no statistical variation in the volume fraction of austenite found in the AM part as a function of the number of builds and how many times the powder was recycled. The amount of austenite remains consistently between about 40 % and 50 % regardless of either the as-manufactured or stress-relieved condition. A minor effect of the heat treatment for stress relief on the transformation of retained austenite to martensitic-ferritic grains was observed based on a post-hardening condition which caused an increase of the HRC hardness

between the as-manufactured and stress-relieved specimens. This is consistent with other studies in literature [*Starr et al, 2012, Kumpaty et al, 2013, and Rafi et al, 2014*]

4. Conclusions

The objective of this study was to determine the effects of recycling stainless steel (17-4 PH) powder, used in the laser-PBF process, on the mechanical properties of built parts and on powder characteristics. A specific powder mixing strategy was used in this study to simulate industrial practice for reusing powder in AM systems. Mechanical properties of additively manufactured specimens were evaluated and recycled powder properties, such as particle size distribution, morphology, flowability, chemical composition, and microstructure, were evaluated and compared to virgin powder.

Powder morphology did not change during the series of 11 builds. This was assessed in two ways. One, morphology was observed using the SEM instrument where no change was visually detected. Second, the dynamic digital image analysis instrument did not detect a change in the aspect ratio of powder within the size range of up to 50 □m.

Powder microstructure was assessed using X-ray diffraction. For powders across the series of builds, the FCC phase was greater than the BCC phase, as expected. The BCC phase peak intensity increased over the series of 11 builds.

The chemical composition of powder during the series of 11 builds did not change except for an increase in carbon despite the powder's exposure in the build chamber to both the laser and the nitrogen environment. Chemical composition of the starting powder correlated well with the chemical composition of the manufactured solid material. After the Build #1, the volume fraction of austenite remained consistent.

Powder size distribution did not significantly change over the series of 11 builds as determined by dynamic digital image analysis. There was a slight and non-significant trend for particle size to decrease as the builds progressed.

Powder flow rate increased with the number of times the powder was recycled. Further evidence that flow rate is related to the number of recycles occurred when virgin powder was introduced to the dispenser bin in Build #5 and a corresponding increase in flow time was measured for the "recycled*" powder for the next Build #6.

Apparent density increased over the series of builds as powder was recycled and, like flow rate, appears to be related to the number of recycles. A decrease in apparent density was measured after virgin powder was introduced in Build #5.

The powder bed density increased with the number of times the powder was recycled. This is consistent with the improved powder flow and increase in apparent density of the powder with recycling, although a change in the powder morphology and a change in powder size distribution was not detected. It would be expected that an increase in fine powder size or an increase in spherical powder would contribute to the improved powder flow, increased apparent density, and PBD.

It is assumed that with an increasing number of recycling steps of the powder in the warm build chamber while it is exposed to the dry and warm nitrogen gas atmosphere, the moisture content of the powder decreases. Decreased humidity may be a reason for an improvement in the flowability, an increase of the apparent density, and in the PBD as well.

There was not a significant change in surface roughness in either the xy- or the xz- plane over the series of builds. The surface was rougher using the R_a or R_z parameter on the xz-plane than on the xy- plane which is expected based on the direction of the build process applying layers in the positive z direction.

The bulk density of manufactured cubes was within 99.5% of the expected density as stated by the machine manufacturer. However, there was not a significant change in density with increasing amount of recycled powder during the series of builds.

Hardness (HRC) did not change with increasing amounts of recycled powder. The hardness of specimens, heat treated for stress relief, was significantly greater when compared to non-heat-treated, as-manufactured, specimens.

No significant change in the mechanical properties of manufactured specimens was observed over the series of builds with multiple times recycled powder. The mechanical properties for the whole series of builds exceeded the minimum property values as reported by the powder supplier.

It seems the driving force that affects the material microstructure are the temperature conditions and duration during the PBF process and during the post heat treatment. Using the machine vendor recommended heat treatment for stress relief results in an increase of the mechanical strength of S17-4 PH compared to the "as-manufactured" S17-4 PH according to the machine vendor material data sheet [*EOS, 2009*].

Tracking recycled powder based on the number of builds may not be the most effective method for tracking recycled powder. A new metric may be required that includes a ratio of accumulated exposure time to powder volume. The accumulated exposure time is the time that the powder is exposed to the laser during the various phases of the build process for a series of builds. Powder volume is a measurement of the amount of powder required to manufacture the part. The use of this ratio will be the topic of further research. Such a new general metric may be independent of the process parameters used and therefore may allow a comparison of recycled powder from different laser-based PBF systems.

Acknowledgment

References

Abrassart, F., 1973; "Stress-induced $\gamma \rightarrow \alpha$ martensitic transformation in two carbon stainless steels. Application to trip steels," *Metallurgical and Materials Transactions B, Volume 4, Issue 9, pp. 2205 – 2016.*

Al-Bermani, S.S., Blackmore, M.L., Zhang, W., Todd, I., 2010, *"The Origin of Microstructural Diversity, Texture, and Mechanical Properties in Electron Beam Melted Ti-6Al-4V," Metallurgical and Materials Transactions A, Volume 41A, 3422-3434.*

ASM Specialty Handbook Stainless Steels, 1994, *Metallurgy and Properties of Wrought Stainless Steels, ASM International Materials Park, OH, p. 13.*

ASTM A564 / ASTM A564M, 2013, Standard Specification for Hot-Rolled and Cold-Finished Age-Hardening Stainless Steel Bars and Shapes, *ASTM International, West Conshohocken, PA.*

ASTM B212, 2015, Standard Practices for Sampling Metal Powders, *ASTM International, West Conshohocken, PA.*

ASTM B213,2013, Standard Test Methods for Flow Rate of Metal Powders Using the Hall Flowmeter Funnel, *ASTM International, West Conshohocken, PA.*

ASTM B527,2015, Standard Test Method for Tap Density of Metal Powders and Compounds, *ASTM International, West Conshohocken, PA*

ASTM E18, 2016, Standard Test Methods for Rockwell Hardness of Metallic Materials1, 2, *ASTM International, West Conshohocken, PA.*

ASTM E1019, 2011, Standard Test Methods for Determination of Carbon, Sulfur, Nitrogen, and Oxygen in Steel, Iron, Nickel, and Cobalt Alloys by Various Combustion and Fusion Techniques, *ASTM International, West Conshohocken, PA.*

ASTM E1086, 2014, Standard Test Method for Analysis of Austenitic Stainless Steel by Spark Atomic Emission Spectrometry, *ASTM International, West Conshohocken, PA.*

ASTM E1876 Standard Test Method for Dynamic Young's Modulus, Shear Modulus, and Poisson's Ratio by Impulse Excitation of Vibration, 2015, *ASTM International, West Conshohocken, PA.*

ASTM E8/E8M Standard Test Methods for Tension Testing of Metallic Materials, 2013, *ASTM International, West Conshohocken, PA.*

ASTM F2792 Standard Terminology for Additive Manufacturing Technologies, 2012, *ASTM International, West Conshohocken, PA.*

Averyanova, Maria, Eugen Cicala, Philippe Bertrand, and Dominique Grevey. 2012. "Experimental Design Approach to Optimize Selective Laser Melting of Martensitic 17-4 PH Powder: Part I – Single Laser Tracks and First Layer." *Rapid Prototyping Journal 18 (1): 28–37.*

E.C. Abdullah, D. Geldart, 1999, "The use of bulk density measurements as flowability indicators," *Powder Technology, Volume 102, 151–165.*

Bhaduri, A. K., Sujith, S., Srinivasan, G., Gill, T. P. S., and Mannan, S. L., 1995; "Optimized Postweld Heat Treatment Procedures for 17-4 PH Stainless Steels," *Welding Research Supplement I, pp. 153-159.*

Blackwell, P.L., 2005, "Mechanical and microstructural characteristics of laser-deposited IN718", *Journal Materials Processing Technology, Volume 170: pp. 240-246.*

Cheruvathur, S., Lass, E. A., and Campbell, C, 2012, "Additive Manufacturing of 17-4 PH Stainless Steel: Post-processing Heat Treatment to Achieve Uniform Reproducible Mircostructure," *Journal of the Minerals, Metals & Material Society (TMS), ISSN: 1047-4838 (Print) 1543-1851 (Online).*

Dingal, S., Pradhan, T.R., Sarin Sundar, J.K., Choudhury, A.R., Roy, S.K., 2009, "The application of Taguchi's method in the experimental investigation of the laser sintering process," *International Journal Additive Manufacturing Technology, Volume 38, pp. 904-914.*

Engeli, R., T. Etter, S. Hövel, and K. Wegener, 2016, "Processability of Different IN738LC Powder Batches by Selective Laser Melting." *Journal of Materials Processing Technology* 229 (March): *pp. 484–491.*

EOS material data sheet for GP1, 2009, EOS GmbH – Electro Optical Systems.

EOS mill test certificate, MTC, S17-4PH, F491201 GP1, 2013, EOS Finland.

Gu, H., Gong, H., Pal, D., Rafi, K., Starr, T., and Stucker, B., 2013; "Influences of Energy Density on Porosity and Microstructure of Selective Laser Melted 17-4PH Stainless Steel," *International Solid Freeform Fabrication Symposium, University of Texas, Austin, USA, pp. 474-489.*

Gu, H., Gong, H., Dilip, J.J.S., Pal, D., Hicks, A., Doak, H., Stucker, B., 2015, "Effects of powder variation on the microstructure and tensile strength of Ti-6Al-4V parts fabricated by selective laser melting," *International Journal of Powder Metallurgy, Volume 51, Issue 1, pp. 35-42.*

ISO 13322-1:2014; Particle size analysis – Image analysis methods – Parts 1: Static image analysis methods, *International Organization for Standardization, Geneva, Switzerland.*

ISO 13322-2:2006; Particle size analysis – Image analysis methods – Part 2: Dynamic image analysis methods, *International Organization for Standardization, Geneva, Switzerland.*

ISO 3369:2006; Impermeable sintered metal materials and hardmetals -- Determination of density, *International Organization for Standardization, Geneva, Switzerland.*

ISO 9276-1:2012; Representation of results of particle size analysis - Part 1: Graphical representation, *International Organization for Standardization, Geneva, Switzerland.*

ISO/ASTM 52921:2013(E) Standard Terminology for Additive Manufacturing— Coordinate Systems and Test Methodologies, *International Organization for Standardization, Geneva, Switzerland and ASTM International, West Conshohocken, PA.*

Jacob, G., Donmez, A., Slotwinski, J., Moylan, S.; 2016, "Measurement of powder bed density in powder bed fusion additive manufacturing processes," *Measurement Science and Technology, Volume 27.*

Jelis, E., Clemente, M., Kerwien, S., Ravindra, N.M., Hespos, M.R.; 2015, "Metallurgical and Mechanical Evaluation of 4340 Steel Produced by Direct Metal Laser Sintering," *The Journal of the Minerals, Metals & Materials Society, Volume 67, Issue 3, pp. 582–589.*

Karapatis, N.P., Egger, G., Gygax, P.E., Glardon, R., 1999, "Optimization of powder layer density in selective laser sintering", *International Solid Freeform Fabrication Symposium, University of Texas, Austin, USA, pp. 255-264.*

Kruth J.P., Levy G., F. Klocke F., and Childs T.H.C.; 2007, "Consolidation phenomena in laser and powder-bed based layered manufacturing", *CIRP Annals – Manufacturing Technology, Volume 56, Issue 2, pp. 730-760.*

Kumpaty, S., Kamara, S., Tomlin, B., Yoo, J., Kumpaty, H., Anderson, D., Govindaraju, M., Kanoongo, N., and Balasubramanian, K.; 2013, "Effect of Heat Treatment on Mechanical/Metallurgical Properties of Direct Metal Laser Sintered 17-4 Precipitate Hardened Stainless Steel," *Advanced Material Research, ISS: 1662-8985, Volume 699, pp. 795-801*

Liu, B., R. Wildman, C. Tuck, I. Ashcroft, and R. Hague, 2011, "Investigation the Effect of Particle Size Distribution on Processing Parameters Optimization in Selective Laser Melting Process," *Annual International Solid Freeform Fabrication Symposium. University of Texas at Austin, Austin, pp. 227–38.*

Murr, E. L., Martinez, E., Hernandez, J., Collins, S., Amato, K. N., Gaytan, S. M., and Shindo, P. W., 2012, "Microstructure and Properties of 17-4 PH Stainless Steel Fabricated by Selective Laser Melting." *Journal of Material Research and Technology, 2012: 1(3), pp. 167-177.*

Nandwana, P., Peter, W.H., Dehoff, R.R., Lowe, L.E., Kirka, M.M., Medina, F., Babu, S.S.; 2016, "Recyclability Study on Inconel 718 and Ti-6Al-4V Powders for Use in Electron Beam Melting," *Metallurgical and Materials Transactions B, Volume 47B., pp 754-762.*

Seidel, Wolfgang, 2001; Werkstofftechnik, Werkstoffe – Eigenschaften – Pruefung – Anwendung, *Carl Hanser Verlag Muenchen Wien, ISBN 3-446-21-28-5: pp 125-135.*

Olakanmi, E.O., 2013, "Selective laser sintering/melting (SLS/SLM) of pure Al, Al-Mg, and Al-Si powders: Effect of processing conditions and powder properties," *Journal of Materials Processing Technology 213: pp. 1387-1405.*

Rafi, K.H., Deepanker, P., Patil, N., Starr, T.L., and Stucker B.E., 2014, "Microstructure and Mechanical Behavior of 17-4 Precipitation Hardable Steel Processed by Selective Laser Melting," *Journal of Material Engineering and Performance, Volume 23(12), pp. 4421 – 4425.*

Slotwinski, J.A., Garboczi, E.J., Stutzman, P.E., Ferraris, C.F., Watson, S.S., Peltz, M.A., 2014, "Characterization of Metal Powders Used for Additive Manufacturing," *Journal of Research of NIST, 119: pp. 460-493.*

Spierings, A.B., Herres, N., Levy, G., 2011, "Influence of the particle size distribution on surface quality and mechanical properties in AM steel parts," *Rapid Prototyping Journal, 17/3, pp. 195-202.*

Spierings, A.B., Levy, G., 2009, "Comparison of density of stainless steel 316L parts produced with selective laser melting using different powder grades," *Annual International Solid Freeform Fabrication Symposium. University of Texas, Austin.*

Starr, T. L., Rafi, K. H., Stucker, B. E., and Scherzer, C. M., 2012, "Controlling Phase Composition in Selective Laser Melted Stainless Steels," *Annual International Solid Freeform Fabrication Symposium, University of Texas, Austin, pp. 439-446.*

Sun, Y.Y., Gulizia, S., Oh, C.H., Doblin, C., Yang, Y.F., Qian, M., 2015, "Manipulation and Characterization of a Novel Titanium Powder Precursor for Additive Manufacturing Applications," *Journal of Metals (JOM), 67/3: pp. 564-572.*

Tang, H.P., Qian, M., Liu, N., Zhang, X.Z., Yang, G.Y., Wang, J., 2015, "Effect of Powder Reuse Times on Additive Manufacturing of Ti-6Al-4V by Selective Electron Beam Melting," *Journal of Metals (JOM)*, 67/3: *pp. 555-563.*

Vilaro, T., Colin, C., and Bartout, J.D., 2011, "As Fabricated and Heat Treated Microstructures of the Ti-6Al-4V Alloy Processed by Selective Laser Melting," *Metall. Mater. Trans. A, pp. 3190-3199.*